J. Fluid Mech. (2019), *vol.* 862, *pp.* 1029–1059. © Cambridge University Press 2019
doi:10.1017/jfm.2018.1017

Exact coherent states of attached eddies in channel flow

Qiang Yang[1,3], Ashley P. Willis[2] and Yongyun Hwang[3,†]

[1]State Key Laboratory of Aerodynamics, China Aerodynamics Research and Development Centre, Mianyang 621000, PR China

[2]School of Mathematics and Statistics, University of Sheffield, Sheffield S3 7RH, UK

[3]Department of Aeronautics, Imperial College London, South Kensington, London SW7 2AZ, UK

(Received 8 August 2018; revised 6 November 2018; accepted 11 December 2018; first published online 16 January 2019)

A new set of exact coherent states in the form of a travelling wave is reported in plane channel flow. They are continued over a range in Re from approximately 2600 up to 30 000, an order of magnitude higher than those discovered in the transitional regime. This particular type of exact coherent states is found to be gradually more localised in the near-wall region on increasing the Reynolds number. As larger spanwise sizes L_z^+ are considered, these exact coherent states appear via a saddle-node bifurcation with a spanwise size of $L_z^+ \simeq 50$ and their phase speed is found to be $c^+ \simeq 11$ at all the Reynolds numbers considered. Computation of the eigenspectra shows that the time scale of the exact coherent states is given by h/U_{cl} in channel flow at all Reynolds numbers, and it becomes equivalent to the viscous inner time scale for the exact coherent states in the limit of $Re \to \infty$. The exact coherent states at several different spanwise sizes are further continued to a higher Reynolds number, $Re = 55\,000$, using the eddy-viscosity approach (Hwang & Cossu, *Phys. Rev. Lett.*, vol. 105, 2010, 044505). It is found that the continued exact coherent states at different sizes are self-similar at the given Reynolds number. These observations suggest that, on increasing Reynolds number, new sets of self-sustaining coherent structures are born in the near-wall region. Near this onset, these structures scale in inner units, forming the near-wall self-sustaining structures. With further increase of Reynolds number, the structures that emerged at lower Reynolds numbers subsequently evolve into the self-sustaining structures in the logarithmic region at different length scales, forming a hierarchy of self-similar coherent structures as hypothesised by Townsend (i.e. attached eddy hypothesis). Finally, the energetics of turbulent flow is discussed for a consistent extension of these dynamical systems notions to high Reynolds numbers.

Key words: turbulent boundary layers, turbulence theory

1. Introduction

The logarithmic dependence of mean velocity profile is the most fundamental feature in wall-bounded turbulent shear flow. The original derivation of von Kármán (1930) is based on the mixing length hypothesis (Prandtl 1925) for modelling of

† Email address for correspondence: y.hwang@imperial.ac.uk

https://doi.org/10.1017/jfm.2018.1017 Published online by Cambridge University Press

Reynolds shear stress in a pressure-driven plane channel flow. Since the mixing length in the region close to the wall ($y/h < 0.2$, where y is the wall-normal direction and h is the half-height of the channel) has to vanish at the wall, the only possible length scale in this region becomes the distance from the wall (i.e. y). Given that the mixing length is conceptually identical to the mean free path in thermodynamics, this indicates that the correlation length scale of fluid motions (i.e. integral length scale) in the logarithmic region would be the distance from the wall. Townsend (1956, 1976) hypothesised that it would be difficult to imagine the emergence of this feature, unless the size of energy-containing eddies (coherent structures) in the logarithmic region is proportional to the distance from their centre to the wall, and, in this sense, these energy-containing eddies should be 'attached' to the wall (i.e. the attached eddy hypothesis). He further assumed that these energy-containing eddies are self-similar and that their near-wall behaviour could be modelled in the inviscid limit. By linearly superposing a generic form of second-order statistical moment of each of the self-similar energy-containing eddies subject to the constant Reynolds shear stress, he predicted that the turbulence intensity of wall-parallel velocity components would be a logarithmically dependent function in the wall-normal direction. For the past two decades, there has been growing evidence that supports the attached eddy hypothesis, and, in particular, recent measurements have confirmed that the theoretical prediction of Townsend (1976) is indeed a reliable first approximation of turbulence intensities in the logarithmic region (e.g. Marusic *et al.* 2013). For further details, the reader may refer to the recent review by Marusic & Monty (2019) and the references therein.

In the original theory of Townsend (1976), the detailed form and dynamical feature of individual attached eddies are not required to construct the logarithmic wall-normal dependence of turbulence intensity of wall-parallel velocity components, because the attached eddies are characterised only by the second-order 'statistical moments'. Indeed, in earlier studies, the form of the attached eddies was modelled only in a statistical manner by taking the flow field observations available at the time. For example, Townsend (1976) himself proposed a double-cone vortex as a statistical model of individual attached eddies from the experimental observation by Kline *et al.* (1967) on the near-wall streaks. In the refining work by Perry & Chong (1982), a 'Λ'-shaped vortex was adopted from the flow visualisation of Head & Bandyopadhay (1981) in a turbulent boundary layer. More recently, Woodcock & Marusic (2015) considered a fairly generic statistical model of attached eddies, given in the form of spanwise alternating streamwise velocity with finite streamwise size.

Nevertheless, the question of what the main energy-containing eddies really are is very important, as these eddies would play the central role in momentum and mass transfer due to their energy-containing nature – indeed, it was recently shown that the energy-containing eddies which scale with the distance from the wall are the dominant source of turbulent skin-friction generation at high Reynolds numbers (de Giovanetti, Hwang & Choi 2016). Recently, some important statistical and dynamical features of these main energy-containing eddies have also been reported. In particular, the energy-containing eddies in the logarithmic region have been repeatedly found to be statistically and dynamically self-similar (Hwang 2015; Hellstöm, Marusic & Smits 2016; Hwang & Bengana 2016), as hypothesised by Townsend (1976). These energy-containing eddies have a sustaining mechanism essentially independent of those at other (length and time) scales (Hwang & Cossu 2010*b*, 2011). Each of the energy-containing eddies is composed of elongated streaks and vortex packets statistically in the form of quasi-streamwise vortices (Hwang 2015; Hwang & Bengana

https://doi.org/10.1017/jfm.2018.1017 Published online by Cambridge University Press

2016), and its turnover dynamics is remarkably similar to the so-called 'self-sustaining process' of near-wall turbulence that involves both linear and nonlinear mechanisms within the given scale (Hamilton, Kim & Waleffe 1995; Waleffe 1997; Schoppa & Hussain 2002). It is important to note that this statistical and dynamical description of the energy-containing eddies integrates all the known coherent structures within the framework of the attached eddy hypothesis (Hwang 2015), including near-wall streaks (Kline *et al.* 1967) and quasi-streamwise vortices (Jeong *et al.* 1997) in the near-wall region, self-similar vortex packets and their wakes in the logarithmic region (del Álamo *et al.* 2006), and large-scale (Kovasznay, Kibens & Blackwelder 1970) and very-large-scale motions in the outer region (Kim & Adrian 1999; del Álamo & Jiménez 2003; Hutchins & Marusic 2007).

The self-sustaining process has been firmly understood as the turbulence generation mechanism, which involves a two-way interaction between streaks and quasi-streamwise vortices (Hamilton *et al.* 1995; Waleffe 1997): quasi-streamwise vortices significantly amplify streaks via the 'lift-up' effect (Butler & Farrell 1993; del Álamo & Jiménez 2006; Cossu, Pujals & Depardon 2009; Pujals *et al.* 2009; Hwang & Cossu 2010*a*; McKeon & Sharma 2010; Willis, Hwang & Cossu 2010), and the amplified streaks subsequently regenerate new quasi-streamwise vortices via streak instability/transient growth and the following nonlinear mechanisms (Hamilton *et al.* 1995; Schoppa & Hussain 2002; Park, Hwang & Cossu 2011; Alizard 2015; Cassinelli, de Giovanetti & Hwang 2017; de Giovanetti, Sung & Hwang 2017). Based on this observation, Waleffe (1998, 2001, 2003) computed a set of non-trivial (relative) equilibrium solutions of the Navier–Stokes equations by cleverly imposing the exact mathematical balance in the two-way interactions between streaks and quasi-streamwise vortices. For the last two decades, a large number of such solutions, in the form of stationary/travelling waves and periodic orbits, have been found (Nagata 1990; Waleffe 1998; Kawahara & Kida 2001; Waleffe 2003; Faisst & Eckhardt 2004; Wedin & Kerswell 2004; Hwang, Willis & Cossu 2016, and many others), and their understanding has played a central role in the recent advance in transition and turbulence at low Reynolds number. These solutions are often called 'exact coherent states', and they characterise the state-space skeleton of turbulence at low Reynolds numbers (Gibson, Halcrow & Cvitanovic 2008; Willis, Cvitanovic & Avila 2013, 2016; Budanur & Hof 2017).

Given the close relation between the self-sustaining process and exact coherent states, the existence of the self-sustaining process for individual attached eddies of Townsend (1976) indicates that such exact coherent states presumably exist at high Reynolds numbers (Hwang 2015; Hwang & Bengana 2016). Although computation of such exact coherent states itself does not necessarily indicate that they can be easily reassembled to form invariant solutions for the entire hierarchical organisation of attached eddies with the Navier–Stokes equations, it would at least allow us to gain physical insight into the emergence of such a hierarchy of coherent structures at high Reynolds number. Interestingly, a set of such exact coherent states was very recently reported by Eckhardt & Zammert (2018) in plane Couette flow, and it was obtained by properly rescaling and continuing a pair of equilibrium states (EQ7 and EQ8) in Gibson, Halcrow & Cvitanovic (2009) to high Reynolds number. In the present study, we report a new set of such exact coherent states in channel flow, which emerges in the form of relative equilibrium states (travelling waves). The exact coherent states in the present study are obtained using an overdamped simulation, as in Hwang & Bengana (2016), and they are in different form from those found by Eckhardt & Zammert (2018) in plane Couette flow (see § 3.3). Near the saddle-node

https://doi.org/10.1017/jfm.2018.1017 Published online by Cambridge University Press

point in their spanwise size L_z, this new set of exact coherent states is found to asymptotically scale in viscous inner units, indicating that they are associated with the birth of near-wall structures on increasing Reynolds number. Continuation of these solutions to high Reynolds numbers with an eddy viscosity model (Rawat *et al.* 2015; Hwang *et al.* 2016) further reveals that they underpin the self-sustaining process of self-similar energy-containing eddies in the logarithmic region emerging in the form of Townsend's attached eddies.

This paper is organised as follows. In § 2, the numerical method for computation of exact coherent states in the present study is presented. Bifurcation, flow structure and statistics of these solutions are then presented in § 3 with continuation to high Reynolds numbers. In that section, the relation of the present solutions to the others is also discussed. Finally, in § 4, scaling of these solutions and the use of eddy viscosity are discussed comprehensively with concluding remarks.

2. Numerical methods

2.1. *Simulations*

We consider a pressure-driven channel flow, in which the streamwise, wall-normal and spanwise directions are denoted by x, y and z, respectively, and they are interchangeably denoted by x_1, x_2 and x_3. The velocity components in these directions are u, v and w, or u_1, u_2 and u_3. The computations in the present study are carried out using the Navier–Stokes solver `Diablo`, which is well documented in Bewley (2014). In this solver, the streamwise and spanwise directions are discretised using Fourier series with 2/3 dealiasing rule, whereas the wall-normal direction is discretised using second-order central differences. Time integration is performed semi-implicitly by combining the Crank–Nicolson method with a third-order Runge–Kutta method. All the computations in the present study are carried out by imposing a constant volume flow rate across the channel.

Further to direct numerical simulations, a set of overdamped large-eddy simulations is considered by implementing the static Smagorinsky model (Smagorinsky 1963) in the manner of our previous studies (Hwang & Cossu 2010*b*, 2011; Hwang 2015; Hwang & Bengana 2016), i.e.

$$\tilde{\tau}_{ij} - \frac{\delta_{ij}}{3}\tilde{\tau}_{kk} = -2\nu_t \tilde{S}_{ij}, \tag{2.1a}$$

with

$$\nu_t = (C_s\tilde{\Delta})^2 \tilde{\mathscr{S}}\mathscr{D}, \tag{2.1b}$$

where $\tilde{\cdot}$ denotes the filtered quantity, S_{ij} the strain-rate tensor, C_s the Smagorinsky constant, $\tilde{\Delta} = (\tilde{\Delta}_1\tilde{\Delta}_2\tilde{\Delta}_3)^{1/3}$ the nominal filter width, $\tilde{\mathscr{S}} = (2\tilde{S}_{ij}\tilde{S}_{ij})^{1/2}$ the norm of the strain-rate tensor, and $\mathscr{D} = 1 - \exp[-(y^+/A^+)^3]$ the van Driest damping function, with $A^+ = 25$ (the superscript $^+$ denotes scaling with viscous inner units, i.e. normalisation by friction velocity u_τ and viscous inner length scale $\delta_\nu (\equiv \nu/u_\tau)$, where ν is the kinematic viscosity). Here, the Smagorinsky constant C_s is the main control parameter of such an overdamped simulation: its artificial elevation has been used to remove smaller-scale background turbulence, while modelling their role in turbulent transport and dissipation with the artificially elevated eddy viscosity (Hwang & Cossu 2010*b*). In the present study, this approach is adopted to continue the discovered exact coherent states to higher Reynolds numbers, and the relevance of this approach will be discussed in detail in § 4.2.

https://doi.org/10.1017/jfm.2018.1017 Published online by Cambridge University Press

In plane channel flow, the spanwise integral length scale of fully developed turbulence typically varies from $\lambda_z^+ \simeq 100$ to $\lambda_z/h \simeq 1.5$ (Hwang 2015). Therefore, setting the spanwise computational domain L_z to be a value between the two spanwise integral length scales eliminates any motions with spanwise size greater than L_z (Hwang 2013). Combining this approach with elevation of C_s by an appropriate value enables us to isolate self-sustaining motions at $\lambda_z = L_z$, as was shown in Hwang (2015) and Hwang & Bengana (2016), where these self-sustaining motions were found to be approximately self-similar with respect to the spanwise length scale λ_z. Since the goal of the present study is to compute a family of exact coherent states embedded in such self-similar motions, the spanwise domain size L_z is set as the main control parameter to characterise the size of exact coherent states. The streamwise domain size is subsequently set to be $L_x = 2L_z$, so that the computed exact coherent states fit in the minimal unit for the self-sustaining process of each energy-containing motion in the logarithmic region (Hwang & Cossu 2011; Hwang & Bengana 2016).

2.2. *Exact coherent states*

The search for exact coherent states is carried out in the following invariant subspace of the velocity fields:

$$[u, v, w, p](x, y, z) = [u, -v, w, p](x, 2h - y, z), \tag{2.2a}$$

$$[u, v, w, p](x, y, z) = [u, v, -w, p](x - L_x/2, y, -z). \tag{2.2b}$$

Here, equation (2.2*a*) corresponds to the mirror symmetry about the channel mid-plane at $y = h$, which is imposed by applying a symmetric boundary condition to the channel centre, $\partial u/\partial y = 0, \quad v = 0, \quad \partial w/\partial y = 0$ at $y = h$. This approach enables us to save computational cost, and also prevents any complications originating from the interaction between the upper and lower parts of the channel (Neelavara, Duguet & Lusseyran 2017). Equation (2.2*b*) corresponds to the so-called 'shift–reflect' symmetry, which is imposed in order to seek an exact coherent state featured with 'sinuous-mode' streak instability. We note that the sinuous-mode streak instability has recently been found as the dominant breakdown mechanism of streaks in the self-sustaining process (Cassinelli *et al.* 2017; de Giovanetti *et al.* 2017). Furthermore, performing a numerical simulation in the minimal flow unit subject to this symmetry was previously found not to yield any significant difference in turbulence statistics from those without this symmetry (Hwang *et al.* 2016).

A travelling-wave form of exact coherent state (i.e. a relative equilibrium) has been sought by combining the Newton–Krylov–Hookstep method (Viswanath 2007; Willis *et al.* 2013) with the numerical solver described in § 2.1. This method computes invariant solutions of the Navier–Stokes equations by minimising the relative error between an initial state and that state time stepped an interval T and shifted in the streamwise direction by a distance $-s_x$. For a travelling wave, the choice of T is arbitrary, and $TU_{cl}/h = 10$–20 is chosen in the present study (U_{cl} is the centreline velocity of the laminar base flow with the same flow rate). The solutions in the present study are computed to a relative-error tolerance of 10^{-6} between the initial and shifted end states. The stability of the computed exact coherent state is also examined by computing its eigenvalues by Arnoldi iteration.

The initial guess for the Newton iteration is directly obtained from an overdamped large-eddy simulation. The spanwise computational domain for this simulation is chosen to be $L_z/h = 0.5$ (thus $L_x/h = 1.0$), and the Reynolds number ($Re \equiv U_{cl}h/\nu$)

https://doi.org/10.1017/jfm.2018.1017 Published online by Cambridge University Press

considered is $Re = 55\,000$. The Smagorinsky constant is set to $C_s = 0.35$, the use of which isolates the self-sustaining motion at the given spanwise length scale. A converged exact coherent state is found from this state by Newton iteration. Numerical continuation of this solution with a pseudo-arclength method is subsequently performed, gradually lowering Re and C_s, until it becomes an exact solution of the Navier–Stokes equations (i.e. $C_s = 0$) at a sufficiently low Reynolds number ($Re \simeq 4000$) for the given computational domain ($L_z/h = 0.5$). Taking this solution as the base case, a set of exact solutions of the Navier–Stokes equations is obtained for a range of L_z and Re (see § 3.1). This task is carried by continuing with L_z and Re, and this differs from the approach by Eckhardt & Zammert (2018), who employed a rescaling approach for a given solution to generate a new solution at different scale. Continuations in the present study are carried out in one parameter at a time, first in either L_z or Re while keeping the other fixed. The continuation parameter is repeatedly switched to collect the data over the range of the two-parameter space. Keeping $C_s = 0$, the smallest spanwise domain continued is $L_z/h = 0.19$, at which $Re = 30\,000$ is reached. While gradually decreasing L_z, further elevation of Re appears to be feasible. This is not attempted, however, as it would require an additional increase of the number of the wall-normal grid points.

Continuation of the discovered exact solutions of the Navier–Stokes equations is typically limited to relatively low Reynolds numbers. As expected, this is particularly true for the solutions with relatively large L_z. However, to explore their relation to the self-sustaining process in the logarithmic region (see § 3.2), they need to be continued to fairly high Reynolds numbers, at which the logarithmic layer of the full simulation would be reasonably well developed. For this purpose, the exact solutions for $L_z/h = 0.375$, 0.5 and 0.75, obtained at low Reynolds numbers ($Re < 10\,000$), are further continued to $Re = 55\,000$ using the overdamped large-eddy simulations described in § 2.1, as in the previous studies (Rawat *et al.* 2015; Hwang *et al.* 2016) – the continuation to $Re = 55\,000$ is performed, while also increasing C_s in (2.1*b*) to an appropriate value. The full simulation at $Re = 55\,000$ yields $Re_\tau \simeq 2000$ ($Re_\tau \equiv u_\tau h/\nu$) for a sufficiently large computational domain (i.e. $L_z > 1.5h$ and $L_x > 3h$ (see also Hwang & Bengana 2016)).

The resolution of exact coherent states in this study is determined carefully. Given the expected self-similarity of the solutions with respect to the horizontal domain size, the number of grid points in the horizontal plane is maintained to be $N_x \times N_z = 36 \times 36$ at all the domains considered. At the same time, the solutions are expected to be localised in the near-wall region (see figure 1*b–d*), thereby requiring a large number of grid points in the wall-normal direction. For the solutions admitted by the Navier–Stokes equations (i.e. $C_s = 0$), two wall-normal resolutions were originally considered for the lower half-channel, i.e. $N_y = 97$ and $N_y = 129$, both of which are stretched using a hyper-tangential function. These resolutions are the typical wall-normal resolutions used for direct numerical simulations at $Re_\tau \simeq 392$ and $Re_\tau \simeq 590$, respectively (see e.g. Moser, Kim & Mansour 1999), and $N_y = 97$ is found to be good enough for most of the parameters considered (see appendix A). Therefore, throughout the present study, we present the result obtained with $N_y = 97$. In the case of the solutions continued to high Reynolds number using the overdamped large-eddy simulation (i.e. with non-zero C_s), the standard wall-normal resolution required for the wall-resolved large-eddy simulation at $Re_\tau \simeq 2000$ is used for consistency with Hwang & Bengana (2016) (i.e. $N_y = 65$). We note that this relatively small number for the wall-normal resolution at such a high Reynolds number is not a great limitation, as the eddy viscosity in (2.1*b*) smooths out the solution. Furthermore, the use of the eddy viscosity is introduced

https://doi.org/10.1017/jfm.2018.1017 Published online by Cambridge University Press

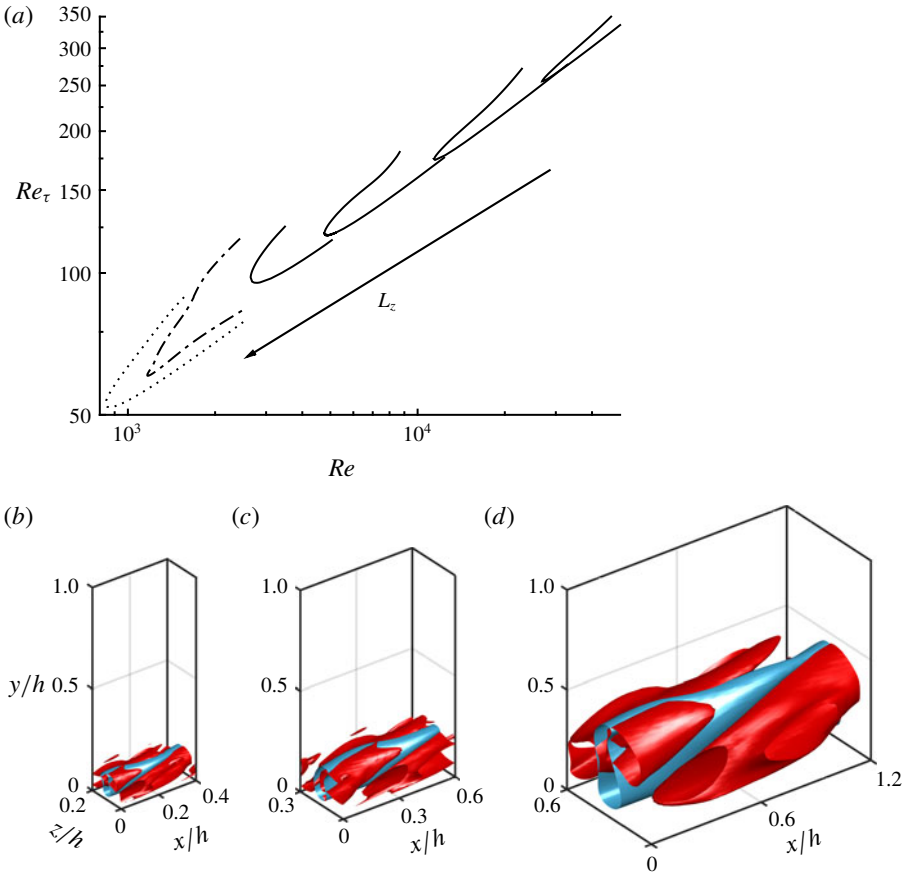


FIGURE 1. (Colour online) Bifurcation of the solutions with respect to Re: (*a*) bifurcation curves for $L_z/h = 0.2,\ 0.3,\ 0.45$ and 0.6; (*b–d*) the corresponding flow visualisations of the saddle-node points at $L_z/h = 0.2,\ 0.3$ and 0.6, respectively. In (*a*), the solutions from Waleffe (2001) and Hwang *et al.* (2016) are presented for $L_z/h = 1.5$: – – – –, Waleffe (2001); · · · · ·, Hwang *et al.* (2016); ——, present study. In (*b–d*), the blue and red isosurfaces indicate $u'^+ = -2$ and $\lambda_2^+ = -0.002$, respectively.

essentially to model the effect of surrounding turbulence, and, as such, any different kind of such models can be adopted for the same purpose. In this respect, the use of the eddy viscosity may be viewed to be *ad hoc*, but we shall see in § 4.2 that its use is inevitable for an energetically consistent description of coherent structures in a turbulent flow.

3. Results

3.1. *Bifurcation and scaling*

Bifurcation of the computed exact coherent states with Re is reported in figure 1(*a*) for various spanwise domain sizes: $L_z/h = 0.2,\ 0.3,\ 0.45$ and 0.6. Here, Re_τ is defined by the friction velocity of each solution, and is introduced to the skin friction of each solution at different Reynolds numbers. In this figure, the travelling-wave solutions, previously obtained by Waleffe (2001) (dash-dotted line) and by Hwang *et al.* (2016)

https://doi.org/10.1017/jfm.2018.1017 Published online by Cambridge University Press

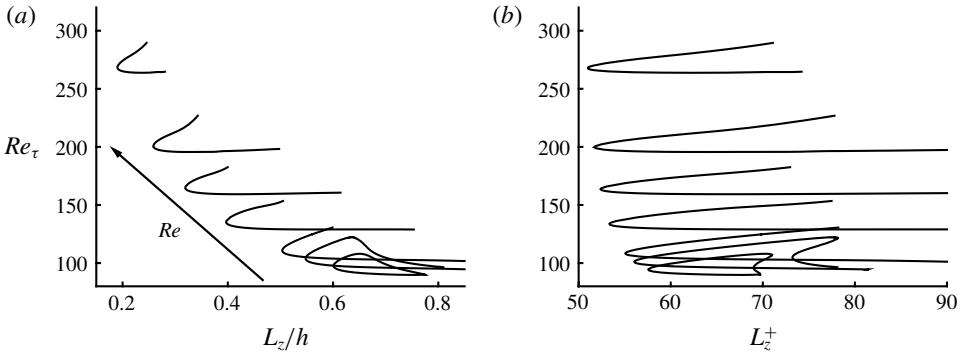


FIGURE 2. Friction Reynolds number of the solutions with respect to (*a*) the outer- and (*b*) the inner-scaled spanwise domains at $Re = 2646$, 3163, 3762, 6250, 10 000, 15 710 and 30 000.

(dotted line), are reported together for $L_z = 1.5h$. We note that these previous solutions also satisfy the symmetries given by (2.2), although they are found unlikely to be connected to the family of solutions reported here (see § 3.3). For given L_z, each set of the solutions shows a saddle-node bifurcation with Reynolds number: the solution that emerges at the saddle-node point divides into two, one of which becomes a high-drag state (upper branch) and the other becomes a low-drag state (lower branch). The flow structure at the onset for different L_z is also shown in figure 1(*b–d*). It is evident that, the smaller the L_z of the solution, the more localised it is to the wall. All the solutions are characterised by a 'wavy' streak (blue isosurfaces of streamwise velocity fluctuations) with sinuous-streak instability and streamwise vortices on the flank (red isosurfaces of the second largest eigenvalue λ_2 of the symmetric tensor $S_{ik}S_{kj} + \Omega_{ik}\Omega_{kj}$, where S_{ij} and Ω_{ij} are the symmetric and antisymmetric parts of the velocity gradient tensor, respectively (Jeong & Hussain 1995)), indicating their physical connection to the self-sustaining process.

Bifurcation of the solutions is also studied with the outer-scaled spanwise domain size L_z/h, as shown in figure 2(*a*) for $Re = 2646$, 3163, 3762, 6250, 10 000, 15 710 and 30 000 ($C_s = 0$). For each Reynolds number, the solutions emerge via a saddle-node bifurcation upon increasing L_z (the left critical point of each bifurcation curve in figure 2), i.e. the solution, emerged at critical L_z, is divided into the upper-branch (high-drag) and lower-branch (low-drag) states. Interestingly, in the case of the two lowest Reynolds numbers considered, these lower- and upper-branch states meet each other again, and they cannot be continued beyond a domain size greater than a certain value ($L_z/h \simeq 0.8$ for $Re = 2646$, and $L_z/h \simeq 0.85$ for $Re = 3163$). However, in general, it is not evident whether such a behaviour would also be observed for the solutions found at higher Reynolds numbers, as their continuation was found to be numerically very difficult while maintaining the relative-error tolerance of 10^{-6} in the Newton iteration.

Given the wall-localised nature of these solutions, it is also appropriate to rescale the size of these structures near the saddle-node point with viscous inner length, as presented in figure 2(*b*). For all Reynolds numbers considered, the smallest inner-scaled spanwise domain ($L_z^+ = Re_\tau L_z/h$) of each solution is found to have similar values, although it should be noted that the saddle-node point is not defined at this domain size – the saddle-node point is defined at the minimal L_z/h of the solution.

https://doi.org/10.1017/jfm.2018.1017 Published online by Cambridge University Press

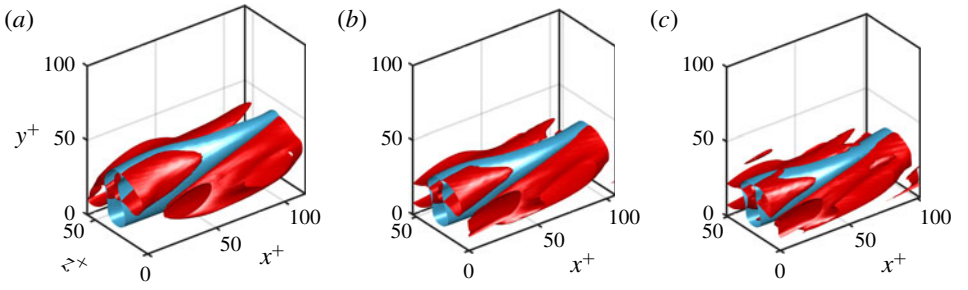


FIGURE 3. (Colour online) Inner-scaled flow visualisation of the solutions at the smallest L_z^+: (*a*) M1, (*b*) M4 and (*c*) M7. Here, the blue and red isosurfaces indicate $u'^+ = -2$ and $\lambda_2^+ = -0.002$, respectively.

Case	Re	Re_τ	L_z/h	c/U_{cl}	L_z^+	c^+
M1	2 646	93.8	0.615	0.467	57.6	13.2
M2	3 163	100.5	0.558	0.402	56.1	12.6
M3	3 762	108.3	0.509	0.351	55.1	12.2
M4	6 250	133.8	0.399	0.249	53.3	11.6
M5	10 000	163.7	0.320	0.186	52.4	11.4
M6	15 710	199.7	0.259	0.143	51.7	11.2
M7	30 000	267.9	0.190	0.099	51.0	11.0

TABLE 1. Properties of the solutions at the smallest L_z^+ in the bifurcation curve.

The smallest inner-scaled spanwise domains at different Reynolds numbers are found to appear to approach an asymptotic value, $L_z^+ \simeq 50$, as Re is increased. This is also seen in table 1, where the spanwise domain size and the phase speed of the solutions at the smallest inner-scaled spanwise domain are summarised. The smallest spanwise domain being $L_z^+ \simeq 50$ is consistent with the typical spanwise spacing of the near-wall motions (i.e. $\lambda_z^+ \simeq 100$) – it indicates that a chaotic state associated with the near-wall dynamics requires a spanwise size greater than $\lambda_z^+ \simeq 50$, while typical and long-lived self-sustaining near-wall turbulence occurs for $L_z^+ \simeq 100$ (see e.g. Jiménez & Simens 2001; Hwang 2013). The phase speed of these solutions also approaches an asymptotic value of $c^+ \simeq 11$ on increasing Re, having the typical advection velocity ($c^+ \simeq 10$–12) of the near-wall coherent structures (Kim & Hussain 1993). The flow fields at the smallest L_z^+ of the solutions are visualised in figure 3 for three different Reynolds numbers (M1, M4 and M7 in table 1), where their domain size and levels of the flow-field isosurfaces are presented to scale in inner units. The inner-scaled solutions are very similar to each other, as is expected from the data in figure 2(*b*) and table 1.

One-point statistics at the smallest L_z^+ of the solutions are also examined in figure 4. To reveal the asymptotic behaviour clearer, we present the data at $Re = 2646$, 6250, 15 710 and 30 000, such that their Re_τ are spaced roughly in an even manner. Figure 4(*a*) shows the mean velocity profile, which appears to be characterised by two regions. In the region below $y^+ \simeq 25$, the mean velocity scales very well in inner units, as those in the full minimal-flow simulations (Hwang 2013). On the other hand, in the region above $y^+ \simeq 40$ where the flow structure rarely exists, the mean flow is close to a parabola, as is the corresponding laminar base flow. Any non-trivial velocity fluctuations (figure 4*b–d*), Reynolds shear stress (figure 4*e*) and

https://doi.org/10.1017/jfm.2018.1017 Published online by Cambridge University Press

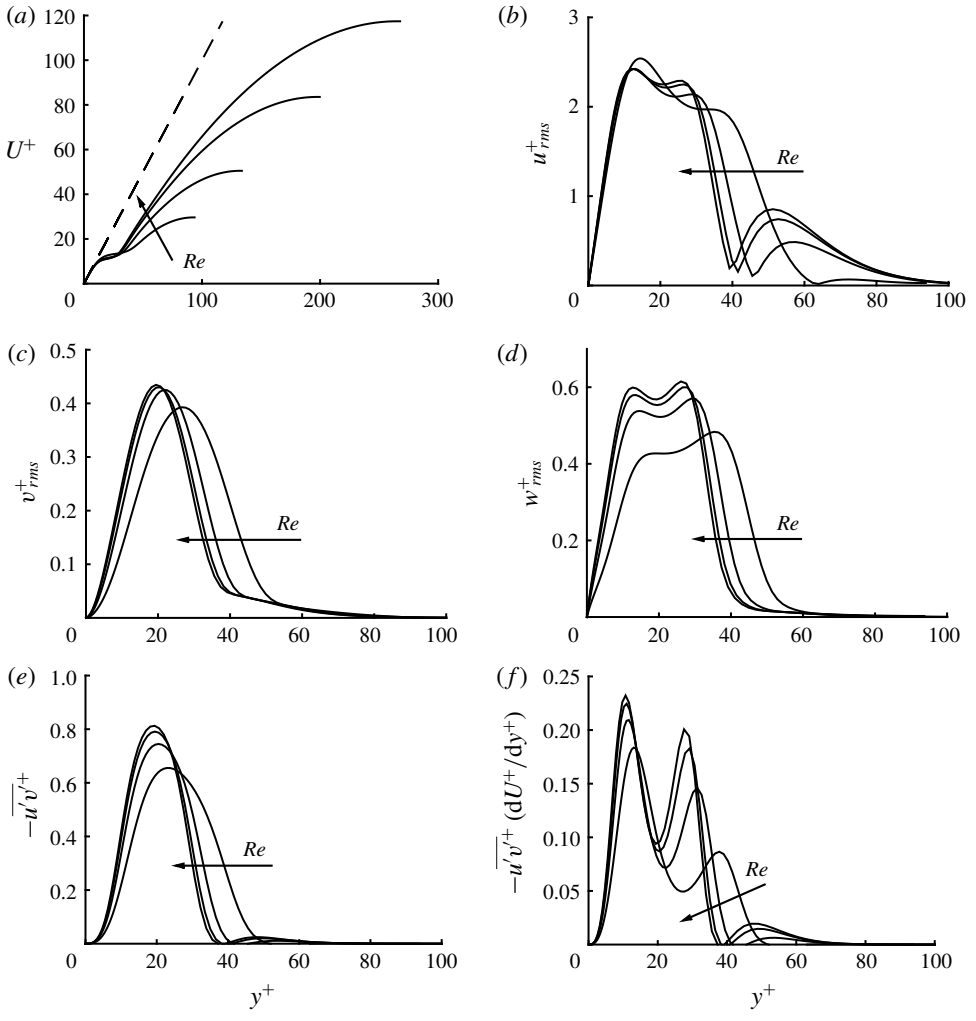


FIGURE 4. Inner-scaled statistics of the solutions at the smallest L_z^+: (*a*) U^+, (*b*) u^+_{rms}, (*c*) v^+_{rms}, (*d*) w^+_{rms}, (*e*) $-\overline{u'v'}^+$ and (*f*) $-\overline{u'v'}^+(\mathrm{d}U^+/\mathrm{d}y^+)$. The Reynolds numbers are $Re = 2646,\ 6250,\ 15\,710$ and $30\,000$. In panel (*a*), the dashed line indicates $U^+ = y^+$.

production (figure 4*f*) appear only in the region below $y^+ \simeq 40$–60. In particular, those obtained from the solutions at the two highest Reynolds numbers are very close to each other, indicating that the solutions indeed approach an asymptotic state approximately independent of the Reynolds number.

In figure 4(*f*), it is also worth noting that turbulence production contains two peaks: one located in the region close to the wall and the other relatively further from the wall. This is not surprising, however, as this feature emerges from the fact that the present exact coherent state is an exact solution of the Navier–Stokes equations. To demonstrate this, let us consider the mean streamwise momentum equation:

$$\frac{\mathrm{d}U^+}{\mathrm{d}y^+} - \overline{u'v'}^+ = 1 - \frac{y^+}{Re_\tau}, \tag{3.1}$$

https://doi.org/10.1017/jfm.2018.1017 Published online by Cambridge University Press

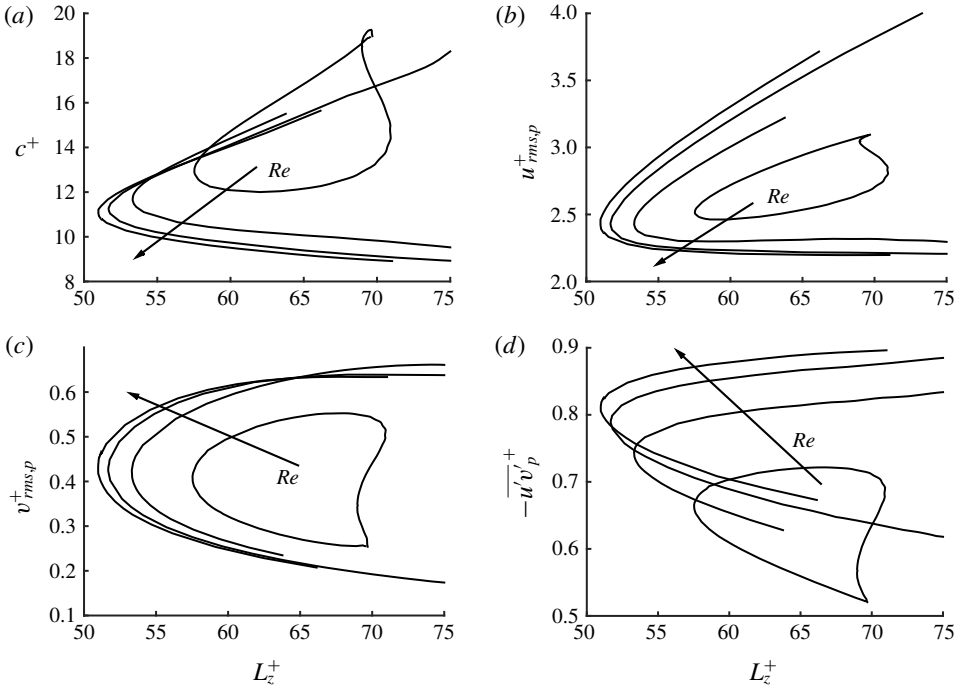


FIGURE 5. Inner-scaled properties of the solutions for $Re = 2646$, 6250, 15 710 and 30 000: (*a*) phase speed, c^+; and peak values of (*b*) u^+_{rms}, (*c*) v^+_{rms} and (*d*) $-\overline{u'v'}^+$. The arrow in each panel passes through the properties of upper-branch states.

where $\bar{\cdot}$ denotes the average in the time and the horizontal directions. In the limit of $Re_\tau \to \infty$, equation (3.1) indicates that the near-wall production (i.e. $-\overline{u'v'}^+(\mathrm{d}U^+/\mathrm{d}y^+)$ below $y^+ \simeq 50$) should have its local maxima at the wall-normal locations where $-\overline{u'v'}^+ = \mathrm{d}U^+/\mathrm{d}y^+ = 1/2$. We note that $-\overline{u'v'}^+ \simeq 1$ in the peak wall-normal location ($y^+ \simeq 20$ in figure 4*e*) and the present exact coherent state is localised around this location. This implies that there would be two wall-normal locations at which $-\overline{u'v'}^+ \simeq 1/2$ if Re_τ is sufficiently large: one appears in the region close to the wall ($y^+ < 20$) and the other is located in the region further from the wall ($y^+ > 20$). This is consistent with the present exact coherent state, which has two wall-normal peaks in the production: the one in the near-wall region resembles that in the turbulent state and the other originates from the wall-localised nature of the present solution.

The upper- and lower-branch states are further characterised in figure 5 using the phase speed c^+, the peak values of velocity fluctuations, and Reynolds shear stress for $Re = 2646$, 6250, 15 710 and 30 000 cases. As in figure 4, the asymptotic behaviour to a universal state is evident especially for the two highest Reynolds numbers considered. Their phase speeds are not very far from $c^+ \simeq 11$, although the ones for lower-branch states are greater than those of upper-branch ones (figure 5*a*). Similar to typical relative equilibria, the peak values of velocity fluctuations indicate that the upper-branch states feature a strong cross-streamwise velocity fluctuation, whereas the lower-branch states have a strong streamwise velocity fluctuation. The upper-branch states also contain larger Reynolds shear stress than the lower-branch ones, as is expected from the identity by Fukagata, Iwamoto & Kasagi (2002) that

https://doi.org/10.1017/jfm.2018.1017 Published online by Cambridge University Press

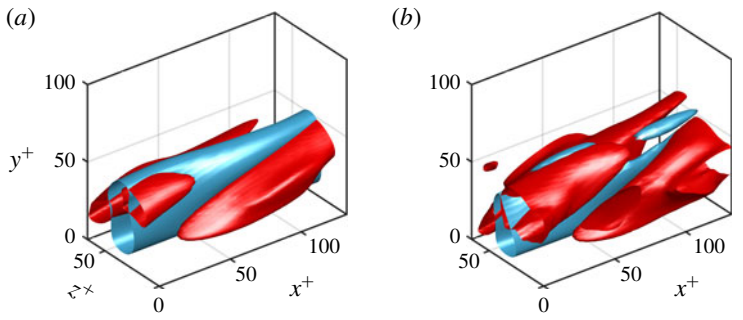


FIGURE 6. (Colour online) Flow visualisation of (*a*) lower- and (*b*) upper-branch states at $Re = 2646$ ($L_z^+ \simeq 65$). Here, the blue isosurface is $u'^+ = -2$, and the red isosurface is $\lambda_2^+ = -0.002$.

directly relates Reynolds shear stress to skin-friction drag. These statistical features are also consistent with the flow fields in figure 6: the upper-branch state exhibits a strong waviness of the streak with more energetic streamwise vortices, whereas the lower-branch one consists of a relatively straight streak and weak streamwise vortices.

The stability of the solutions is examined for the smallest L_z^+ at each Reynolds number (see also figure 2*b*). For this analysis, the eigenvalues of the Navier–Stokes equations linearised about the given travelling-wave solution are computed in the co-moving frame using the Arnoldi algorithm. Figure 7 shows the first five leading eigenvalues computed in the invariant subspace of (2.2). Given the fairly good inner-scaling nature of the exact coherent states, the inner scaling of the computed eigenvalues is first examined in figure 7(*a*). The most unstable eigenvalues of each solution appear to scale reasonably well in inner units. This feature is similar to that of the wall-localised equilibrium states (EQ7 and EQ8) in plane Couette flow (Eckhardt & Zammert 2018), where only a few leading eigenvalues were found to scale in inner units. However, in the present channel flow, such leading eigenvalues are found to scale better with U_{cl} and h, as is further shown in figure 7(*b*). This non-intuitive behaviour needs a more careful examination of the scaling of these leading eigenvalues, and a detailed discussion on this issue will be given in § 4.1. Finally, we observe that the zero eigenvalue here is associated with the streamwise shift of the solution. The zero eigenvalue related to the saddle-node point need not quite be observed here, as the saddle-node point is defined at the minimum L_z/h rather than at the minimum L_z^+.

The two unstable eigenvalues in the form of a complex conjugate pair in figure 7 indicate that the associated instability generates a modulated wave that breaks the following flow symmetry of the given solution:

$$[u, v, w, p](x, y, z, t) = [u, v, w, p](x - ct, y, z, 0). \tag{3.2}$$

Focusing on $Re = 6250$, we further investigate the behaviour of the eigenspectra by continuing the solution in L_z from the lower- to the upper-branch state. In figure 8, we present a root locus analysis by tracking a few most unstable modes with the continuation (note that the neutral eigenvalues with non-zero imaginary parts in figure 7 were not included in this analysis). The behaviour of the first type (i.e. the leading two eigenvalues in figure 7) is shown in figure 8(*a*). Two purely real eigenvalues in figure 7 are found to collide with each other and form a complex

https://doi.org/10.1017/jfm.2018.1017 Published online by Cambridge University Press

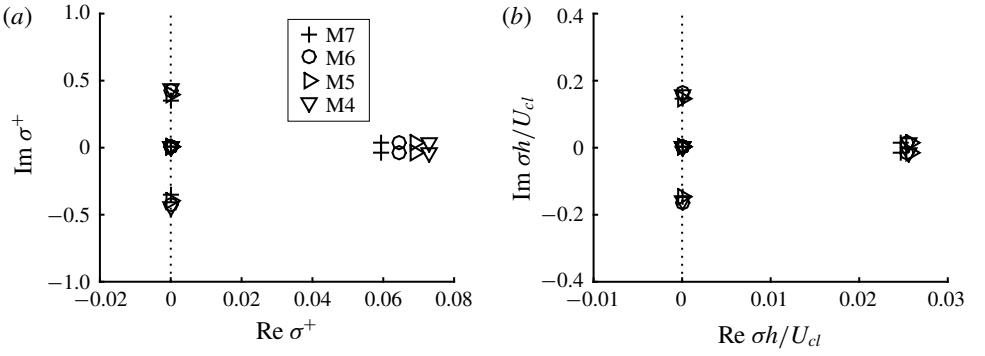


FIGURE 7. Eigenspectra of the solutions at the smallest L_z^+: (*a*) σ^+ and (*b*) $\sigma h/U_{cl}$, where σ denotes the eigenvalues.

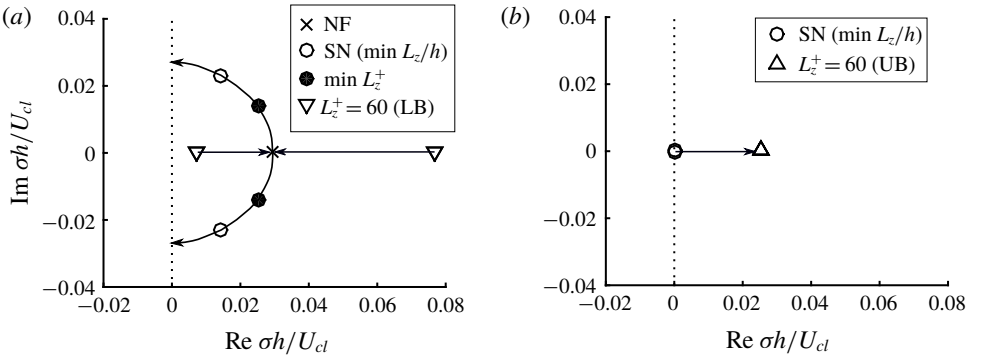


FIGURE 8. Root loci of unstable modes of the present exact coherent state at $Re = 6250$: (*a*) first two modes exhibiting a node-focus transition; (*b*) second mode with a single eigenvalue that becomes neutral at the saddle-node point. The arrows indicate the direction of the root loci from lower- to upper-branch state. Here, SN and NF indicate saddle-node and node-focus point, respectively.

conjugate pair of eigenvalues, indicating a node-focus transition, as the solution is continued from the lower- to the upper-branch state. The complex conjugate pair of eigenvalues become neutral with a further continuation, indicating the formation of a limit cycle through a Hopf bifurcation. The behaviour of this mode is reminiscent of that reported for a travelling-wave solution in pipe flow (Mellibovsky & Eckhardt 2011). However, it is important to note that these eigenvalues do not cross zero at the saddle-node point (i.e. at the minimum L_z/h in figure 2*a*); thereby it is difficult to directly relate them to Takens–Bogdanov bifurcation. Indeed, another eigenmode is found to be related to the saddle-node bifurcation, shown in figure 8(*b*). This mode becomes unstable as the solution moves from the lower- to the upper-branch state. In particular, the zero crossing takes place exactly when the solution reaches the saddle node, consistent with the saddle-node bifurcation in figure 2(*a*).

3.2. *Continuation to high Reynolds numbers*

The exact coherent states discussed in the previous section are localised in the wall-normal direction, while scaling well with inner units near their critical Reynolds

https://doi.org/10.1017/jfm.2018.1017 Published online by Cambridge University Press

Case	L_z/h	C_s	Re_τ	c/U_{cl}	c/U_c	U_c/U_{cl}
LB1	0.375	0.3	664	0.31	0.31	1.00
UB1	0.375	0.3	789	0.22	0.21	1.06
LB2	0.5	0.32	789	0.38	0.39	0.98
UB2	0.5	0.32	989	0.29	0.28	1.04
LB3	0.75	0.35	1039	0.48	0.51	0.95
UB3	0.75	0.35	1415	0.40	0.40	1.00

TABLE 2. Parameters of the solutions continued to $Re = 55\,000$ using overdamped large-eddy simulations. Here, U_c denotes the centreline mean velocity of each solution.

numbers. In this section, we will show that these states evolve into those relevant to the logarithmic region, as Reynolds number is increased. The exact solutions of the Navier–Stokes equations for $L_z/h = 0.375$, 0.5 and 0.75, obtained at low Reynolds numbers ($Re < 10\,000$) in § 3.1, are continued to $Re = 55\,000$ while maintaining the given L_z. At this Reynolds number, the separation between the inner and the outer length scale is reasonably clear, and thus it is possible to identify physically meaningful structures associated with the logarithmic region. The three domain sizes are deliberately chosen to match the minimal attached eddies in the logarithmic region studied by Hwang & Bengana (2016). This numerical continuation is carried out while gradually increasing both Re and C_s. The target value of the Smagorinsky constant C_s for each L_z is chosen by carefully monitoring the one-dimensional spanwise wavenumber spectra of the corresponding overdamped simulation, such that only the largest admissible eddy survives in the given flow domain. We note that the turbulence statistics of these overdamped simulations for different L_z are found to exhibit self-similarity with L_z, as reported previously in Hwang (2015) and Hwang & Bengana (2016) (not shown here).

Table 2 summarises the parameters and properties of the solutions continued to $Re = 55\,000$ using the overdamped large-eddy simulation. Here, we note that the friction velocity of all the solutions is smaller than $Re_\tau \simeq 1800$, the value expected from a full simulation at this Re for a sufficiently large computational domain (i.e. $L_x \gtrsim 3h$ and $L_z \gtrsim 1.5h$) (de Giovanetti *et al.* 2016). This is primarily because the contribution of the structures, the spanwise size of which is greater than the given spanwise domain L_z in table 2, does not exist – see de Giovanetti *et al.* (2016) for further details. For this reason, the friction Reynolds number of the solutions tends to be smaller on decreasing L_z. Finally, the larger L_z is, the larger c/U_{cl} (or c/U_c where U_c is the centreline mean velocity) is found. This is expected because the solution at larger size is located further from the wall in outer units, and is thereby exposed to larger mean advection velocity. However, the mean velocity of each solution is now very different from the original one from a full simulation because the isolation procedure of the flow structures at a given spanwise length scale destroys the Reynolds shear stress carried by the structures at other length scales. Given the direct relation between Reynolds shear stress and mean velocity through the streamwise mean momentum equation (3.1), it is evident that scaling of the phase speed of the solutions would not provide any useful physical insight in relation to the original logarithmic mean velocity. Therefore, this issue has not been pursued any further.

The lower- and upper-branch solutions continued to $Re = 55\,000$ are visualised in figure 9. The levels of the isosurfaces in this figure are scaled by u_τ of each solution

https://doi.org/10.1017/jfm.2018.1017 Published online by Cambridge University Press

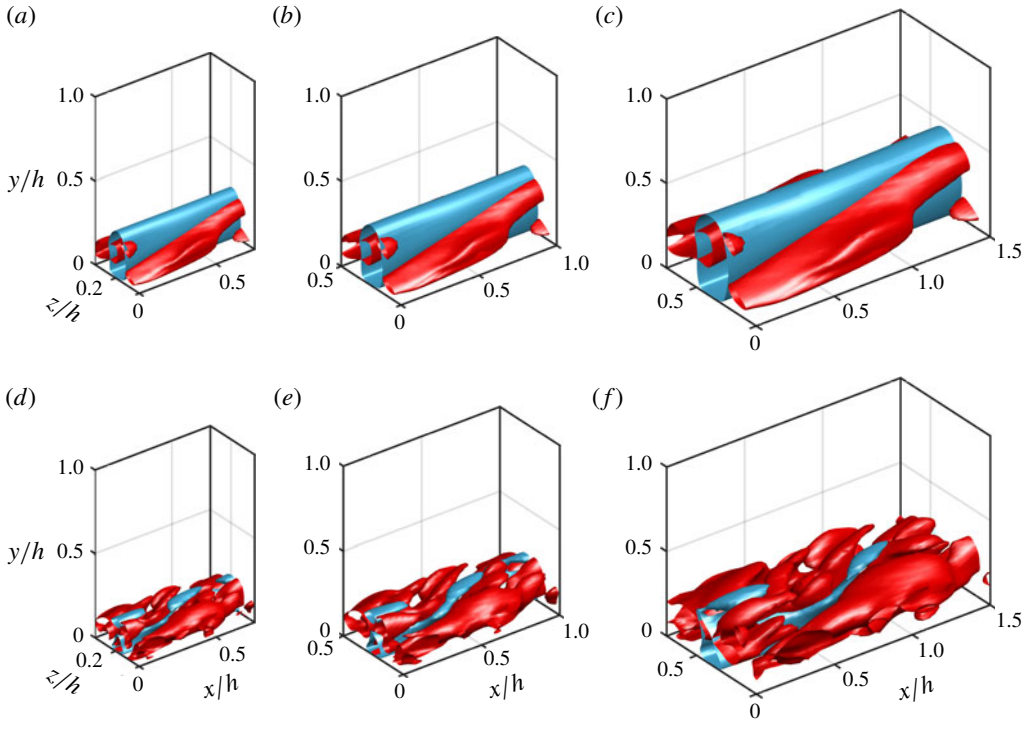


FIGURE 9. (Colour online) Flow visualisation of (*a–c*) the lower- and (*d–f*) the upper-branch states: (*a,d*) $L_z/h = 0.375$, (*b,e*) $L_z/h = 0.5$ and (*c,f*) $L_z/h = 0.75$. Here, the blue isosurface indicates $u'^{+} = -2.2$ for all the plots, while the red isosurfaces in (*a–c*) are $\lambda_2 = -5(u_\tau/L_z)^2$ and those in (*d–f*) are $\lambda_2 = -20(u_\tau/L_z)^2$.

and its spanwise domain L_z. The flow visualisation reveals that the flow structures of the lower- and upper-branch solutions are roughly self-similar with respect to these scales, while maintaining the typical features of exact coherent states: i.e. the upper-branch solutions contain stronger streamwise meandering motions of the streak and more intense streamwise vortical structures than the lower-branch ones.

The self-similarity of the flow structures can also be seen in the normalised turbulent velocity fluctuations and Reynolds shear stress with respect to L_z, as reported in figure 10. These statistics can be scaled with the peak location of each profile, but the observed self-similarity remains almost unchanged (see appendix B). Since the upper-branch solutions will be shown to be of particular relevance to the self-sustaining turbulent state (see figures 12 and 13), here we focus mainly on statistical features of these solutions. Both the streamwise and spanwise velocity fluctuations of the upper-branch solutions have their primary peaks around the location fairly close to the wall, i.e. $y/L_z \simeq 0.06$–0.07 (figure 10*b*,*f*). These velocity fluctuations are also considerably large in the region close to the wall: for example, at $y/L_z = 0.05$, $u_{rms}/u_{rms,max} \simeq 0.95$ and $w_{rms}/w_{rms,max} \simeq 0.9$. On the other hand, the peak wall-normal locations of the wall-normal velocity fluctuation and Reynolds shear stress are located further from the wall than those of the streamwise and spanwise velocity fluctuations, i.e. $y/L_z \simeq 0.2$–0.25 for wall-normal velocity (figure 10*d*) and $y/L_z \simeq 0.15$–0.2 for Reynolds shear stress (figure 10*h*). Therefore, both the wall-normal velocity fluctuation and Reynolds shear stress do not reach the region close to the wall. For example, at

https://doi.org/10.1017/jfm.2018.1017 Published online by Cambridge University Press

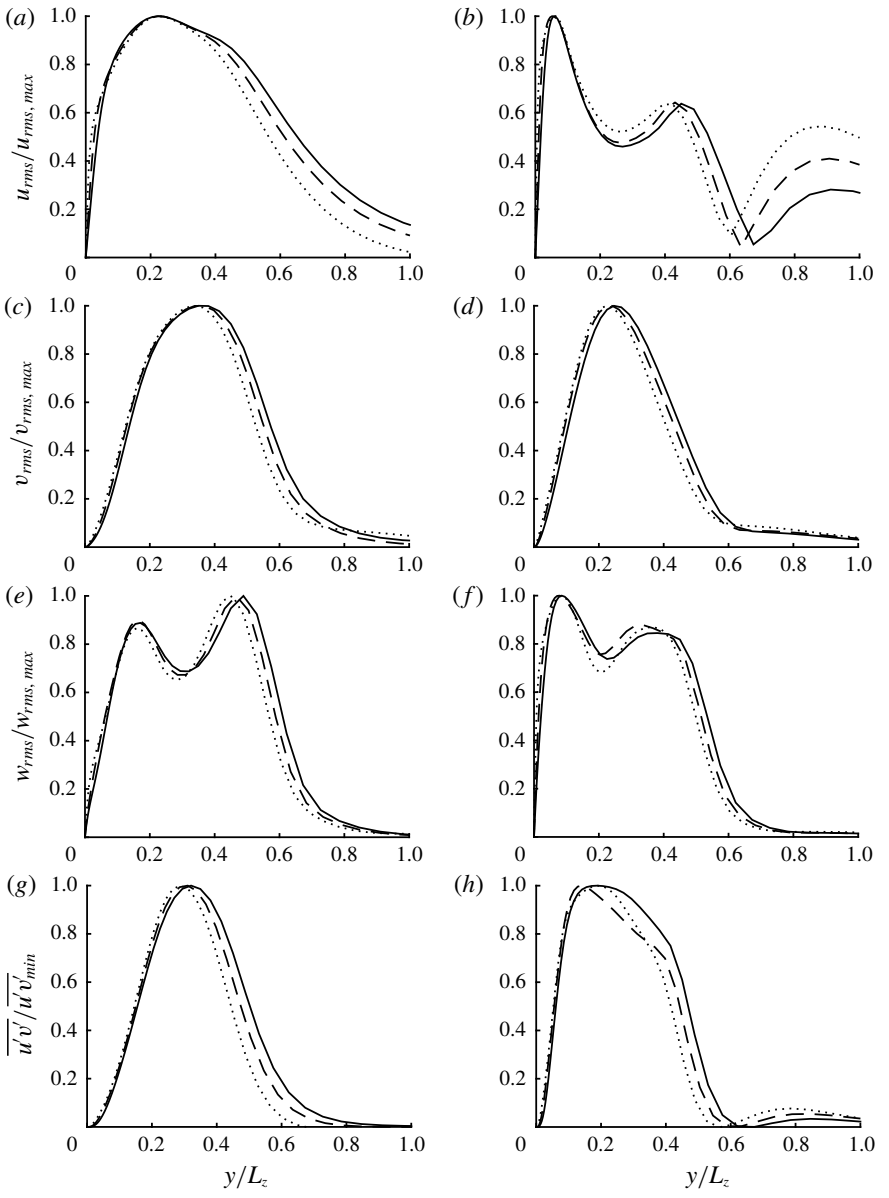


FIGURE 10. Normalised second-order statistics of (*a*,*c*,*e*,*g*) the lower- and (*b*,*d*,*f*,*h*) the upper-branch states with respect to the spanwise domain L_z: (*a*,*b*) streamwise, (*c*,*d*) wall-normal, (*e*,*f*) spanwise velocity and (*g*,*h*) Reynolds shear stress. Here: ——, $L_z/h = 0.375$; – – – –, $L_z/h = 0.5$; · · · · · ·, $L_z/h = 0.75$.

$y/L_z = 0.05$, $v_{rms}/v_{rms,max} \simeq 0.2$ and $\overline{u'v'}/\overline{u'v'}_{min} \simeq 0.4$, which are much smaller than those of $u_{rms}/u_{rms,max}$ and $w_{rms}/w_{rms,max}$.

The self-similarity of the upper-branch solutions with respect to L_z and their near-wall behaviour shown in figure 10 suggest that the statistical features of the upper-branch solutions are consistent with those of an 'individual attached eddy' in Townsend (1976). Furthermore, these upper-branch solutions do appear to contribute

https://doi.org/10.1017/jfm.2018.1017 Published online by Cambridge University Press

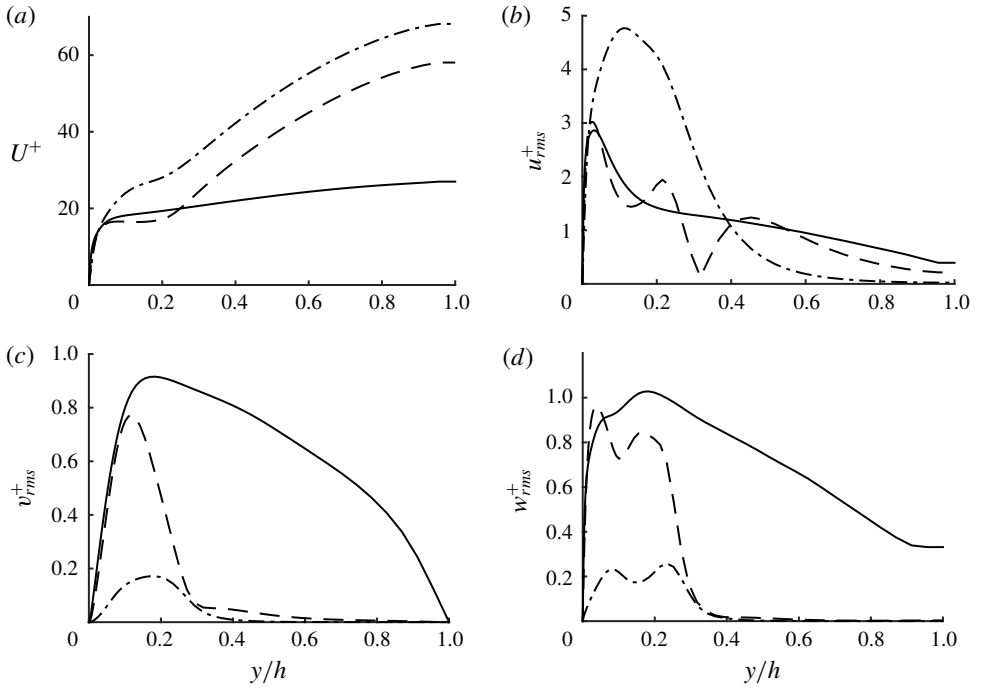


FIGURE 11. First- and second-order statistics for $L_z/h = 0.5$: (*a*) U^+, (*b*) u^+_{rms}, (*c*) v^+_{rms} and (*d*) w^+_{rms}. Here: ——, full simulation; – – – –, upper-branch state (UB2); – – – – –, lower-branch state (LB2).

to the logarithmic region. Since the mean velocity profile is directly coupled with Reynolds shear stress through the streamwise mean-momentum equation, this issue can be explored with the Reynolds shear-stress profile in figure 10(*h*). Note that the spanwise integral length scale in turbulent channel flow is proportional to the distance from the wall for $100\delta_\nu \leqslant L_z \leqslant 1.5h$ (e.g. Hwang 2015). Given the peak wall-normal location of the Reynolds shear stress profiles (i.e. $y/L_z \simeq 0.15$–0.2), the wall-normal locations, to which the peak Reynolds shear stress of the upper-branch solutions contributes, would be in $(15$–$20)\delta_\nu \leqslant y \leqslant (0.2$–$0.3)h$. It is evident that this range is very close to the typical wall-normal extent of the logarithmic layer, suggesting that the upper-branch solutions would indeed be relevant to the logarithmic layer.

The observed statistical self-similarities are also consistent with the statistical data of the overdamped large-eddy simulations in Hwang (2015) and Hwang & Bengana (2016). However, it is found that there is an important difference between the turbulence statistics and the present relative equilibrium states of the overdamped large-eddy simulations. Figure 11 compares first- and second-order statistics of the lower- and upper-branch solutions (LB2 and UB2) with those of the corresponding unsteady simulation for $L_z = 0.5h$ at the same C_s. In the region close to the wall ($y/h < 0.2$) where the exact coherent states carry non-zero turbulent fluctuations, the upper-branch state seems to reasonably describe the statistics of the full chaotic dynamics in the unsteady simulation. However, both upper- and lower-branch states are localised only in the region close to the wall, and, especially, their cross-streamwise velocity components carry very little energy above $y/h \simeq 0.2$. This is in contrast to the full chaotic dynamics of the overdamped large-eddy simulation,

https://doi.org/10.1017/jfm.2018.1017 Published online by Cambridge University Press

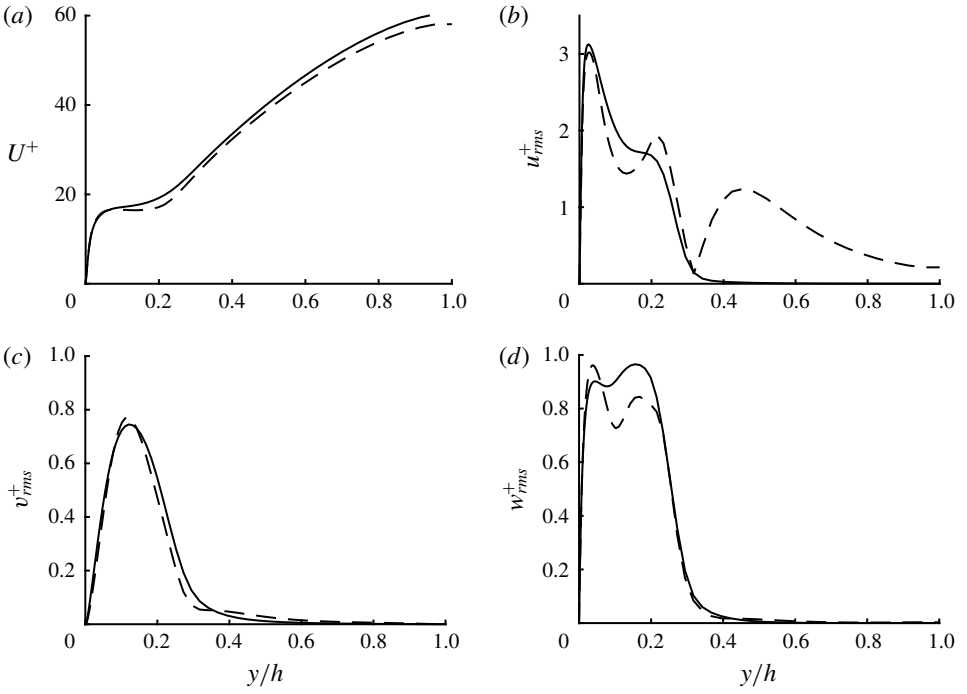


FIGURE 12. First- and second-order statistics for $L_z/h = 0.5$: (*a*) U^+, (*b*) u^+_{rms}, (*c*) v^+_{rms} and (*d*) w^+_{rms}. Here: ——, simulation with damping (3.3); – – – –, upper-branch state (UB2).

because it exhibits fairly large velocity fluctuations above $y/h \simeq 0.2$. It is important to mention that such non-zero turbulent fluctuations for $y/h > 0.2$ were analysed in our recent study for minimal Couette flow (Yang, Willis & Hwang 2018), and they were shown to be the consequence of local mean shear in such an outer region, which admits self-sustaining processes at the length scale of the artificially narrow spanwise domain.

Towards isolating the chaotic dynamics associated mainly with the solutions in the present study, we perform an additional numerical simulation, in which the velocity fluctuations above a certain wall-normal location are artificially damped out. Note that this technique is similar to the one used in Jiménez & Pinelli (1999). We consider the following form of body forcing to the right-hand side of the Navier–Stokes equations:

$$f_i = \mu(y)(u_i - \langle u_i \rangle_{x,z}), \tag{3.3a}$$

where $\langle\cdot\rangle_{x,z}$ indicates the average in the streamwise and spanwise directions and

$$\mu(y) = \mu_0 \left\{ 1 - \frac{1}{2} \left[1 + \tanh\left(10 \left(\frac{\eta^2}{\eta_0^2} - 1 \right) \right) \right] \right\}. \tag{3.3b}$$

Here, μ_0 $(= U_{cl}/h)$ is the damping strength used, $\eta = y/h - 1$, $\eta_0 = y_0/h - 1$, and y_0 is the wall-normal location, above which the damping (3.3) is applied. The location of y_0 is determined by gradually lowering from the centreline until turbulence is not sustained in the domain; this gives $y_0 = 0.6L_z$. Figure 12 compares the first- and second-order statistics of the upper-branch state (UB2) with those of an overdamped

https://doi.org/10.1017/jfm.2018.1017 Published online by Cambridge University Press

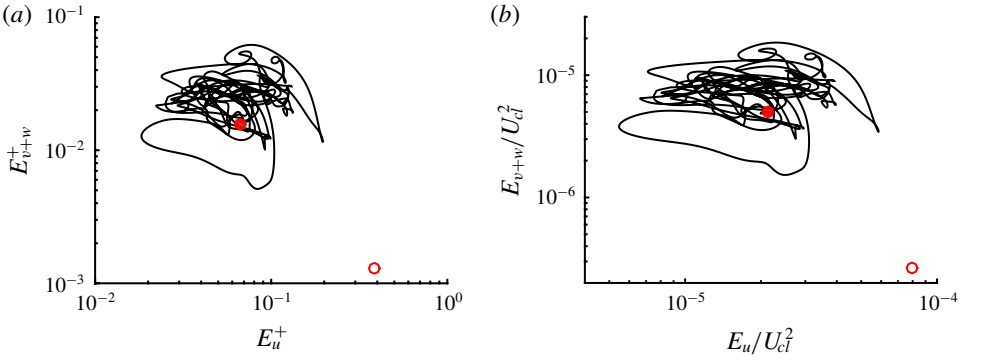


FIGURE 13. (Colour online) Phase portrait for $L_z/h = 0.5$ in the plane of E_u–E_{v+w} scaled in (*a*) inner and (*b*) outer units. Here: ——, simulation with damping (3.3); open circles, LB2; and filled circles, UB2.

simulation with (3.3) ($y_0 = 0.3h$) for $L_z/h = 0.5$. It is evident that the statistics now compare much more favourably with each other (compare figure 12 with figure 11), indicating the upper-branch state as a good proxy of the self-sustaining energy-containing motion below $y/h \simeq 0.3$.

From the simulation with the damping function (3.3), the state-space location of the upper-branch state can be shown. To this end, we consider the following state-space variables:

$$E_u = \frac{1}{2V_{\Omega_n}} \int_{\Omega_n} u'^2 \,\mathrm{d}V, \quad E_{v+w} = \frac{1}{2V_{\Omega_n}} \int_{\Omega_n} v'^2 + w'^2 \,\mathrm{d}V, \tag{3.4}$$

where u', v' and w' are streamwise, wall-normal and spanwise velocity fluctuations, respectively. Here, V_{Ω_n} is the volume of the near-wall region of the computational domain defined as $\Omega_n = [0, L_x] \times [0, 0.6L_z] \times [0, L_z]$, and this is introduced to consider only the region where both the damped simulation and the solutions continued with the eddy viscosity carry non-negligibly large velocity fluctuations (note that energy input and dissipation have not been considered as the dissipation of the damped simulation requires incorporation of the contribution from the damping body force in (3.3), whereas the solutions do not). In figure 13, the phase portraits respectively scaled by u_τ and U_{cl} in the E_u–E_{v+w} plane are shown. In both cases, the upper-branch state is reasonably well placed in the middle of the chaotic solution trajectory given by the self-sustaining motion at the given size, suggesting that the upper-branch state would be a reasonable proxy for the near-wall chaotic dynamics and its skin-friction generation in the damped simulation.

3.3. *Relation to other solutions*

The relative equilibrium states in the present study belong to the invariant subspace described by (2.2). The two solutions previously reported by Waleffe (2001) and Hwang *et al.* (2016) also belong to this subspace, although they were computed in different ways: the solution in Waleffe (2001) was obtained by continuously deforming the base flow from the one of Nagata (1990) in plane Couette flow, whereas the solution in Hwang *et al.* (2016) was obtained using an overdamped

https://doi.org/10.1017/jfm.2018.1017 Published online by Cambridge University Press

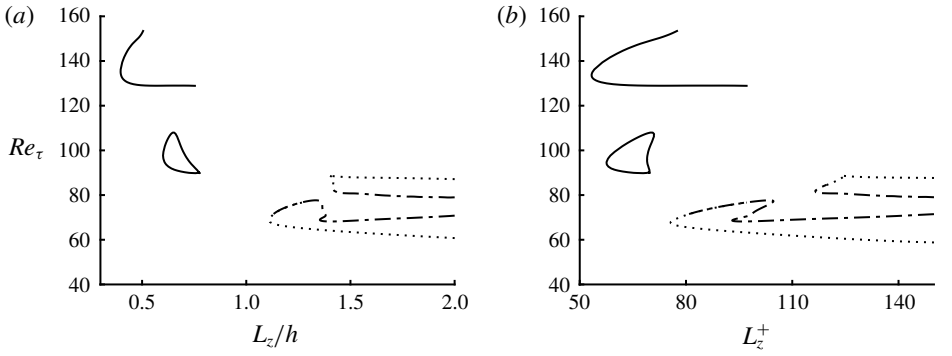


FIGURE 14. (*a*) Outer- and (*b*) inner-scaled bifurcation curves with L_z. Here: – – – –, Waleffe (2001) and · · · · · ·, Hwang *et al.* (2016) at $Re = 1538$; whereas ——, at $Re = 2646$ (lower curve) and $Re = 6250$ (upper curve).

large-eddy simulation designed to isolate self-sustaining large- and very-large-scale motions, the spanwise size of which is $L_z/h \simeq 1.5$ (Hwang & Cossu 2010*b*). In this section, we explore whether the solutions in the present study have any link with these previous solutions. It is useful to remember that the solutions reported in the present study could be continued only for small spanwise domain ($L_z/h \lesssim 1$; see also figure 2), whereas those in Waleffe (2001) and Hwang *et al.* (2016) were previously reported for the spanwise domains larger than $L_z/h \simeq 1$.

First, numerical continuation of the solutions in Waleffe (2001) and in Hwang *et al.* (2016) is performed by gradually lowering L_z. Here, the solution of Waleffe (2001) was obtained by downloading its raw data from his personal webpage. His solution was interpolated onto our grid system, then used as initial condition of our Newton solver. The Newton iteration converged quickly and the retrieved solution using our solver showed excellent agreement with that in Waleffe (2001). The continuation result of the two pairs of the solutions in Waleffe (2001) and in Hwang *et al.* (2016) with L_z is shown in figure 14 at $Re = 1538$. For a sufficiently large spanwise domain ($L_z/h > 1.5$ or $L_z^+ > 140$), the two solution pairs form four equilibrium states. As L_z is decreased, their upper-branch states meet each other around $L_z/h \simeq 1.4$ ($L_z^+ \simeq 120$) and the lower-branch ones exhibit the same behaviour around $L_z/h \simeq 1.2$ ($L_z^+ \simeq 75$). This suggests that the solutions in Waleffe (2001) and in Hwang *et al.* (2016) are homotopic relatives, while implying that they are unlikely to be continued for $L_z \lesssim h$. Furthermore, these solutions are found not to be localised in the near-wall region, as L_z is decreased (not shown here).

By contrast, it is found that the solutions in the present study begin to emerge at a little higher Reynolds number (see the solid line curves at $Re = 2646$ in figure 14). This suggests that the solutions in the present study are unlikely to be continuously or directly linked to those reported in Waleffe (2001) and Hwang *et al.* (2016). However, any possibility of their mutual connections should not be completely ignored at this moment. Indeed, the disappearance of the solutions of Waleffe (2001) and Hwang *et al.* (2016) on decreasing L_z might be linked to the emergence of different types of invariant solutions, such as a relative periodic orbit, through a saddle-node infinite period (SNIPER) bifurcation, as was recently reported in Rawat, Cossu & Rincon (2016) with the solution of Waleffe (2001) for large $L_z(>2h)$ at $Re = 2000$. Such a periodic orbit emerging from the SNIPER bifurcation might be connected to the

https://doi.org/10.1017/jfm.2018.1017 Published online by Cambridge University Press

solutions in the present study, although pursuing this issue any further is beyond the scope of the present study.

Finally, the present solutions are compared with those recently reported by Eckhardt & Zammert (2018) in plane Couette flow. We note that the wall-localised solutions in Eckhardt & Zammert (2018) originate from a pair of the solutions (EQ7 and EQ8) in Gibson *et al.* (2009), and they are obtained by rescaling the Navier–Stokes equations with its spanwise domain size using the uniform base-flow shear of plane Coutte flow. While their solutions were found to scale in inner units as those in the present study, it appears that their spatial structure is significantly different from the present solutions in plane channel flow. For example, the EQ7 and EQ8 solutions in Gibson *et al.* (2009) typically exhibit two pairs of streaks and quasi-streamwise vortices, and the high- and low-speed streaks alternate along the streamwise directions. By contrast, the spatial structure of the present solution features a pair of high- and low-speed streaks continuously linked along the streamwise direction (figure 6), which is more like the solutions found in Waleffe (2001) and Hwang *et al.* (2016). This suggests that the solutions in the present study are not likely to be homotopic with those in Eckhardt & Zammert (2018).

4. Discussion

4.1. *Scaling of the exact coherent states*

The exact coherent states in the present study have been found to scale approximately in inner units, except their eigenvalues, which appear to scale better with the time scale of the laminar base flow (figure 7*b*). Given the wall-localised nature of these states, this observation is intuitively unexpected, leading us to examine their precise scaling more carefully. To address this issue, it is instructive to consider the equation for the rate of the total kinetic energy per unit volume:

$$\frac{\mathrm{d}E}{\mathrm{d}t} = I - D, \tag{4.1a}$$

where

$$\left.\begin{gathered} E = \frac{1}{2V_\Omega}\int_\Omega u_i u_i \,\mathrm{d}V, \\ I = \frac{U_m \nu}{V_\Omega}\int_0^{L_x}\int_0^{L_z} \left.\frac{\partial u}{\partial y}\right|_{y=0} \mathrm{d}x\,\mathrm{d}z, \quad D = \frac{\nu}{V_\Omega}\int_\Omega \frac{\partial u_i}{\partial x_j}\frac{\partial u_i}{\partial x_j}\,\mathrm{d}V. \end{gathered}\right\} \tag{4.1b}$$

Here, V_Ω $(= L_x \times L_y \times L_z)$ is the volume of the computational domain Ω, I the rate of energy input originating from the applied pressure gradient, D the rate of dissipation, and U_m $(= (2/3)U_{cl})$ the bulk velocity. We first restrict ourselves to the relative equilibrium solutions in the present study. From (4.1), it is evident that the rate of energy input for the given equilibrium state is $I = (U_m/h)u_\tau^2$. Unless the dissipation mechanism imposes different velocity and time scales, the velocity scale of the kinetic energy E should become u_τ with the evolution time scale given by $T_e = h/U_m$. This is expected to be particularly true near the critical Reynolds number at which the solutions emerge, because their integral and dissipation scales are expected to be hardly separated. Indeed, at the saddle-node point of the solutions, we have shown that the velocity fluctuations scale well with u_τ (e.g. figure 5) and that the leading eigenvalues in figure 7 scale well with T_e (equivalently to h/U_{cl} with the factor 3/2).

https://doi.org/10.1017/jfm.2018.1017 Published online by Cambridge University Press

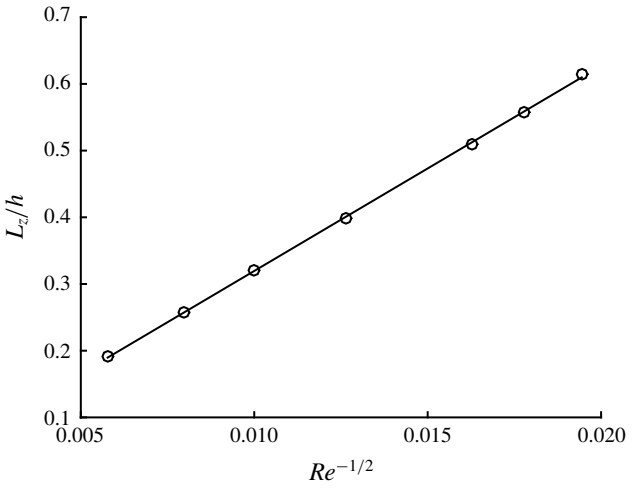


FIGURE 15. Scaling of the critical spanwise domain L_z at the onset of the exact coherent states with respect to $Re^{-1/2}$.

At first glance, this observation, made with (4.1) and figure 7(*b*), is seemingly odd because T_e is the time scale of fluid motion which travels downstream with the 'bulk' velocity U_m over the 'outer'-scaling distance h. Indeed, it is intuitively difficult to imagine how any wall-localised fluid motion, such as the solutions in the present study, would scale with such a global time scale T_e instead of the local viscous inner time scale $T_{in} = \nu/u_\tau^2$. However, there is also further evidence supporting T_e as the time scale of the solutions in the present study. Given the expected little scale separation between the processes of I and D near the saddle-node point of the solutions, the rate of dissipation in this case would scale as $D \sim \nu u_\tau^2/L_z^2$ (L_z is the spanwise size of the solutions). The balance between I and D in (4.1) with $\mathrm{d}E/\mathrm{d}t = 0$ yields the following scaling of the spanwise wavelength with Reynolds number:

$$\frac{L_z}{h} \sim \frac{1}{\sqrt{Re}}, \tag{4.2}$$

providing scaling of the saddle-node point of the exact coherent states in the 'outer unit'. Here, we note again that (4.2) is obtained by setting $I = u_\tau^2/T_e$. In figure 15, (4.2) is examined by plotting the spanwise domain size of each solution at the saddle-node point as a function of $1/\sqrt{Re}$. It is evident that (4.2) provides an excellent prediction for the 'outer' scaling of the spanwise domain size of the saddle-node point with Reynolds number, suggesting that T_e would indeed be the time scale of the present exact coherent states.

All of the observations, made on the time scale of the present exact coherent states, are physically difficult to explain, unless there exists an explicit mathematical relation between T_e and T_{in}. Therefore, we now explore how they are precisely related to each other for the solutions in the present study. In the limit of $Re \to \infty$, the size of the solutions have been shown to asymptotically scale in inner units (i.e. $L_z^+ \simeq$ const., as shown in table 1. Combining this with (4.2) then yields

$$\frac{u_\tau}{U_{cl}} \sim \frac{1}{\sqrt{Re}} \quad \text{and} \quad \frac{\delta_v}{h} \sim \frac{1}{\sqrt{Re}}, \tag{4.3a,b}$$

https://doi.org/10.1017/jfm.2018.1017 Published online by Cambridge University Press

which provide the explicit relation between the inner scales and those of the laminar base flow. It is then straightforward to realise

$$T_e \sim T_{in}, \tag{4.4}$$

indicating that T_{in} is actually proportional to T_e for $Re \to \infty$. This now explains that T_{in} would be the time scale for the solutions, if $Re \to \infty$, and confirms that the relatively poor inner scaling of the eigenvalues in figure 7(*a*) is the finite-Reynolds-number effect of the solutions.

Based on this observation, we now take u_τ and T_{in} as the velocity and time scales, and consider $Re \to \infty$. Then, in this limit, we have that the mean and velocity fluctuations of the exact coherent states in the present study are governed by the following equations:

$$\frac{\mathrm{d}U^+}{\mathrm{d}y^+} - \overline{(u'v')}^+ = 1, \tag{4.5a}$$

$$\frac{\partial u_i'^+}{\partial t^+} + U_j^+ \frac{\partial u_i'^+}{\partial x_j^+} + u_j'^+ \frac{\partial U_i^+}{\partial x_j^+} = -\frac{\partial p'^+}{\partial x_i^+} + \frac{\partial^2 u_i'^+}{\partial x_j^+ \partial x_j^+} - u_j'^+ \frac{\partial u_i'^+}{\partial x_j^+} + \overline{u_j'^+ \frac{\partial u_i'^+}{\partial x_j^+}}, \tag{4.5b}$$

where the overbar denotes average in time, $U_i = U(y)\delta_{i1}$ is the mean velocity, and u_i' and p' are the velocity and pressure fluctuations, respectively. Here the mean equation (4.5*a*) now explicitly excludes the term originating from the mean pressure gradient because $Re_\tau \to \infty$ from (4.3): indeed, if the Reynolds shear stress is zero, (4.5*a*) indicates that the base flow becomes a uniform shear flow, as one would easily expect.

Equations (4.5) now suggest that different types of wall-localised exact coherent states can be further sought using (4.5) rather than the full equations. This would be particularly beneficial from the computational viewpoint, since these exact coherent states do not contain any significant flow structures in most of the wall-normal domain. Furthermore, the viscous term in (4.5) is given at the order of unity, suggesting that such solutions at least at their onset would follow the asymptotic description proposed by Deguchi (2015) with imposition of a no-slip boundary condition at the wall. Finally, the form of the mean equation (4.5*a*) indicates that the full turbulent dynamics of (4.5) is also relevant to description of the dynamics of the so-called 'mesolayer', in which the effect of viscous force from the presence of the wall dominates over that of the pressure gradient. Given the size of the mesolayer scaling as $\Delta y^+ \sim \sqrt{Re_\tau}$ (where Δy^+ is the wall-normal extent of the mesolayer (see Afzal 1982; Sreenivasan & Sahay 1997)), the only additional requirement should be that the size of the computational domain needs to follow $L_{dom} \ll \sqrt{Re_\tau}$, where L_{dom} is the size of computational domain in all the directions.

4.2. *Continuation to high Reynolds numbers with eddy viscosity*

The continuation of the exact coherent states to high Reynolds number in § 3.2 has been carried out by introducing an eddy viscosity, which was implemented using the overdamped large-eddy simulation (e.g. Hwang & Cossu 2010*b*). Introduction of such an artificially elevated eddy viscosity was originally done to examine the self-sustaining processes in the logarithmic and outer regions. However, in the present study, its main benefit lies in enabling us to extend the dynamical systems notions to high Reynolds numbers. In particular, it technically relaxes the numerical difficulty

https://doi.org/10.1017/jfm.2018.1017 Published online by Cambridge University Press

typically arising in continuation of the upper-branch states to high Reynolds numbers, which are highly relevant to the description of the turbulent state. To provide a more comprehensive discussion of the physical relevance of the present eddy-viscosity-based approach, we start by considering the dimensional form of the equations for turbulent fluctuation. Since the size of the coherent structures in fully developed turbulence and the present exact coherent states is well characterised by the spanwise length scale (e.g. Hwang 2015), it is useful to consider a Fourier-mode decomposition of turbulent velocity fluctuation in the spanwise direction:

$$u_i'(t, x, y, z) = \int_{-\infty}^{\infty} \widehat{u_i'}(t, x, y; k_z) \mathrm{e}^{\mathrm{i}k_z z} \, \mathrm{d}k_z, \tag{4.6}$$

where $\widehat{\cdot}$ denotes the Fourier-transformed state and k_z is the spanwise wavenumber. Then, the streamwise-averaged equation for the turbulent kinetic energy at each spanwise wavenumber (i.e. $\widehat{e}(y; k_z) = \widehat{u_i'}(y; k_z)\widehat{u_i'}^{*}(y; k_z)$) is given by

$$\begin{aligned}
\overline{\frac{\partial \widehat{e}(y; k_z)}{\partial t}} = & \underbrace{\left\langle \mathrm{Re}\left\{ -\overline{\widehat{u'}^{*}(y; k_z)\widehat{v'}(y; k_z)} \frac{\mathrm{d}U(y)}{\mathrm{d}y} \right\} \right\rangle_x}_{\widehat{P}(y;k_z)} + \underbrace{\left\langle -\nu \overline{\frac{\partial \widehat{u_i'}(y; k_z)}{\partial x_j} \frac{\partial \widehat{u_i'}^{*}(y; k_z)}{\partial x_j}} \right\rangle_x}_{\widehat{\varepsilon}(y;k_z)} \\
& + \underbrace{\left\langle \mathrm{Re}\left\{ -\overline{\widehat{u_i'}^{*}(y; k_z) \frac{\partial}{\partial x_j} \left(\widehat{u_i' u_j'}(y; k_z) \right)} \right\} \right\rangle_x}_{\widehat{T}_{turb}(y;k_z)} \\
& + \underbrace{\left\langle \mathrm{Re}\left\{ \frac{\mathrm{d}}{\mathrm{d}y} \left(-\overline{\frac{\widehat{p'}(y; k_z)\widehat{v'}^{*}(k_z)}{\rho}} \right) \right\} \right\rangle_x}_{\widehat{T}_p(y;k_z)} + \underbrace{\left\langle \nu \frac{\mathrm{d}^2 \overline{\widehat{e}(y; k_z)}}{\mathrm{d}y^2} \right\rangle_x}_{\widehat{T}_\nu(y;k_z)},
\end{aligned} \tag{4.7}$$

where * denotes the complex conjugate, and $\langle \cdot \rangle_x$ the spatial average in the x-direction. Here, $\widehat{P}(y; k_z)$ is turbulence production, $\widehat{\varepsilon}(y; k_z)$ dissipation, $\widehat{T}_{turb}(y; k_z)$ nonlinear turbulent transport, $\widehat{T}_p(y; k_z)$ transport by pressure, and $\widehat{T}_\nu(y; k_z)$ viscous transport (i.e. diffusion of turbulent kinetic energy). In the region above the wall, $\widehat{T}_p(y; k_z)$ and $\widehat{T}_\nu(y; k_z)$ have been found to be negligible, and they will be excluded in the following discussion on the energetics of coherent structures in the logarithmic region. Also, $\partial \widehat{e}(y; k_z)/\partial t$ goes to zero with the time average. For a further discussion on these issues, the reader may refer to Cho, Hwang & Choi (2018) and Lee & Moser (2019).

Given the scale of turbulent kinetic energy in (4.2) and the logarithmic mean velocity, turbulence production should scale as $\widehat{P}(y; k_{z,int}) \sim u_\tau^3/y$ at the wavenumbers of integral length scales ($k_{z,int} \sim 2\pi/y$) where turbulence production mainly takes place and dissipation is negligibly small. Therefore, from (4.7), the main energy balance at $k_z = k_{z,int}$ is given by

$$\widehat{P}(y; k_{z,int}) + \widehat{T}_{turb}(y; k_{z,int}) \simeq 0, \tag{4.8}$$

as numerically confirmed by, for example, Cho *et al.* (2018). This balance can also be checked by scaling the nonlinear turbulent transport term with the integral velocity and length scales in the logarithmic region (i.e. u_τ and y): $\widehat{T}_{turb}(y; k_{z,int}) \sim O(u_\tau^3/y)$, whereas $\widehat{\varepsilon}(y; k_{z,int}) \sim O(Re_y^{-1} u_\tau^3/y)$ with Re_y $(= u_\tau y/\nu) \to \infty$ by the definition of the

https://doi.org/10.1017/jfm.2018.1017 Published online by Cambridge University Press

logarithmic layer. Therefore, for $k = k_{int}$, the dissipation $\widehat{\varepsilon}$ cannot be balanced with the production $\widehat{P}$, and the only possible way to form the energy balance is through (4.8).

Since turbulent transport is an energy-preserving process over the given computational domain, $\int_{-\infty}^{\infty} \widehat{T}_{turb}(y;\ k_z)\,\mathrm{d}k_z \simeq 0$ in the logarithmic layer (Cho *et al.* 2018). This implies that the negative $\widehat{T}_{turb}(y;\ k_{z,int})$ in (4.8) should be positive at some other k_z. It is evident that this process should take place through energy cascade to dissipate out the produced turbulent kinetic energy. The dissipation process takes place at the Kolmogorov microscale given by $\eta \equiv (\nu^3/\widehat{P}(y;\ k_{z,int}))^{1/4}$, thus $\eta \sim y^{1/4}$ in the logarithmic region. Since turbulence production at the dissipation scales should be negligibly small, the main energy balance at the dissipation length scale (i.e. $k = k_{z,dis}$ $(\sim 2\pi/\eta)$) is given by

$$\widehat{T}_{turb}(y;\ k_{z,dis}) + \widehat{\varepsilon}(y;\ k_{z,dis}) \simeq 0. \tag{4.9}$$

Here, (4.9) is made by approximating the energy-conservative nature of nonlinear turbulent transport (i.e. $\int_{-\infty}^{\infty} \widehat{T}_{turb}(y;\ k_z)\,\mathrm{d}k_z \simeq 0$), such that $\widehat{T}_{turb}(y;\ k_{z,dis}) + \widehat{T}_{turb}(y;\ k_{z,int}) \simeq 0$. From (4.8), one can easily derive

$$\widehat{P}(y;\ k_{z,int}) \simeq \widehat{\varepsilon}(y;\ k_{z,dis}), \tag{4.10}$$

the balance between turbulence production and dissipation in the logarithmic layer (Tennekes & Lumley 1967), which is also consistent with the spectral budget analysis of full numerical simulation data in Cho *et al.* (2018) and Lee & Moser (2019).

Now, let us consider the overdamped large-eddy simulations, in which all the motions, except the self-sustaining one at $k_z = k_{z,int}$, are damped out by artificially increasing C_s in (2.1). It is evident that this artificial elimination of the motions at other scales would significantly reduce the role of nonlinear transport in (4.8), as there are now very few motions to nonlinearly interact with each other. However, the physical dissipation at the integral length scale (i.e. $\widehat{\varepsilon}(y;\ k_{z,int})$) cannot be large at high Reynolds numbers, indicating that the dissipation by the artificially elevated eddy viscosity is replacing the role of $\widehat{T}_{turb}(y;\ k_{z,int})$, such that

$$\widehat{P}(y;\ k_{z,int}) + \widehat{\epsilon}_{\nu}(y;\ k_{z,int}) \simeq 0, \tag{4.11}$$

where $\widehat{\epsilon}_{\nu}(y;\ k_{z,int})$ is the dissipation by the eddy-viscosity model in (2.1). Here, it is important to mention that the replacement of $\widehat{T}_{turb}(y;\ k_{z,int})$ with $\widehat{\epsilon}_{\nu}(y;\ k_{z,int})$ should not change at least the value of $\widehat{P}(y;\ k_{z,int})$. In other words, the friction velocity u_τ should be maintained to be roughly the same in this replacement process, since $\widehat{P}(y;\ k_{z,int}) \sim u_\tau^3/y$. Indeed, the use of (2.1) has been consistently found not to yield any significant change in the friction velocity (see e.g. Hwang 2015), indicating that it does not significantly modify the value of $\widehat{P}(y;\ k_{z,int})$ described by the self-sustaining process and the exact coherent states in the present study. By contrast, an artificial elevation molecular viscosity (i.e. lowering Reynolds number) significantly reduces $\widehat{P}(y;\ k_{z,int})$ as well, because it also involves a significant reduction of the friction velocity.

The discussion here suggests that modelling the surrounding turbulence using an eddy-viscosity-based model, as in the present study, provides an energetically consistent description for the processes at high Reynolds numbers, although it is essentially *ad hoc* to extend the notions of dynamical systems to such regimes. Given this nature, it is also possible to consider any other form of such a model as long as

https://doi.org/10.1017/jfm.2018.1017 Published online by Cambridge University Press

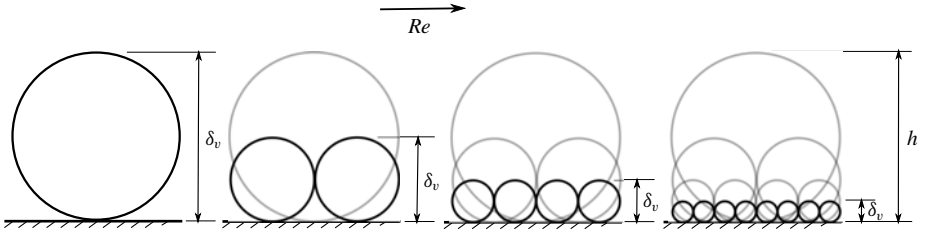


FIGURE 16. A schematic illustration of the evolution of attached eddies in turbulent channel flow. Dark circles indicate attached eddies at the emergence, and grey circles indicate attached eddies evolved from those at lower Reynolds numbers.

it correctly models the energetics described here. In this respect, it is finally worth mentioning the recent phenomenological modelling of coherent structures using the notions of the relative equilibrium (Chini *et al.* 2017), and such a modelling effort may also take some benefit from the energy balance discussed here.

5. Concluding remarks

We have presented a family of exact coherent states, individual members of which appears to underpin the individual attached eddy hypothesised by Townsend (1976). The initial condition for the Newton iteration in the present study was obtained from an overdamped large-eddy simulation with a narrow spanwise computational domain, in which the related energy-containing eddies reside through their self-sustaining process (Hwang & Bengana 2016). Then, a converged exact coherent state of the Navier–Stokes equations was obtained, and the solution family was subsequently calculated by continuing with the spanwise domain size and with Reynolds number. It has been found that these solutions emerge with a scaling in inner units, suggesting that, right after the onset (i.e. the saddle-node point), they underpin the self-sustaining process of near-wall coherent structures. Continuation of these solutions to high Reynolds number, using the overdamped large-eddy simulation (Hwang & Cossu 2010*b*; Hwang 2015), has further revealed that they evolve into the self-similar states in the logarithmic region, each of which underpins the self-sustaining process at its length scale.

This observation for the exact coherent states in the present study indicates that the near-wall region (say $y^+ \leqslant 30$) is the location where new sets of coherent structures are born on increasing Reynolds number, and their size scales in inner units near this onset. With further increase of Reynolds number, the near-wall structure that emerged at different (lower) Reynolds numbers subsequently evolves into the structures in the logarithmic region at different length scales, as illustrated by the schematic in figure 16. It is evident that this process leads the main flow topology in the logarithmic region to become in the form of a hierarchy of self-similar coherent structures, consistent with the attached eddy hypothesis of Townsend (1976). From this perspective, the self-similarity of the coherent structures in the logarithmic region is a natural consequence of this process, as they all initially emerged in the form of near-wall coherent structures at lower Reynolds numbers.

The invariant solutions of the Navier–Stokes equations found in the present study provide solid evidence on the existence of Townsend's attached eddies, each of which would underpin the self-sustaining process of an individual attached eddy at

https://doi.org/10.1017/jfm.2018.1017 Published online by Cambridge University Press

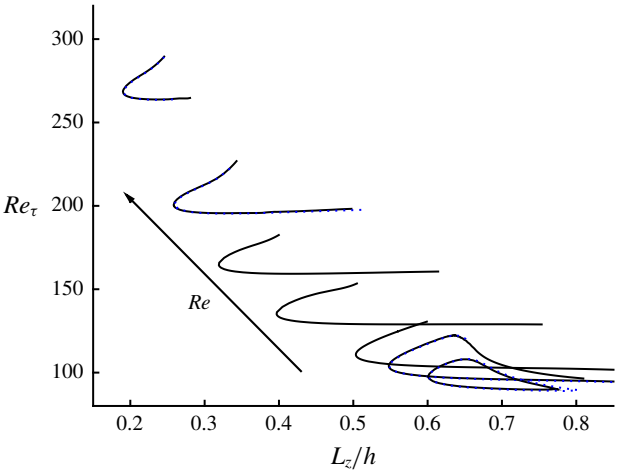


FIGURE 17. Friction Reynolds number of the solutions with respect to the outer spanwise domains at $Re = 2646$, 3163, 3762, 6250, 10 000, 15 710 and 30 000: here: ——, $N_y = 97$; – – – –, $N_y = 129$.

a given length scale. The present result also provides direct support for the previous work conducted with the linearised Navier–Stokes equations where self-similar linear transient-growth/resolvent/proper orthogonal decomposition modes were found (del Álamo & Jiménez 2006; Hwang & Cossu 2010*a*; Moarref *et al.* 2013). Finally, it is tempting to use the statistics of the present exact coherent states as the input for the previous analysis based on linear superposition of statistics of individual attached eddies (e.g. Perry, Henbest & Chong 1986; Perry & Marusic 1995). However, it should be pointed out that the Navier–Stokes equations are nonlinear. Therefore, in principle, such a superposition, which would strictly be valid for the linearly decomposable statistics of the given flow (e.g. Fourier modes), is not feasible with the present solutions, placing a new challenge for a theoretical description of high-Reynolds-number turbulence using invariant solutions. Nevertheless, bifurcation of these states in the present study has provided important physical insight into the fundamental mechanism by which the hierarchical organisation of self-similar coherent structures is formed throughout the logarithmic layer on increasing Reynolds numbers.

Acknowledgements

Q.Y. would like to acknowledge the National Key Research and Development Program of China (2016YFA0401200) and the Natural Science Foundation of China (11802322, 11772350, 11702307). Y.H. was supported by the Engineering and Physical Sciences Research Council (EPSRC) in the UK (EP/N019342/1).

Appendix A. Effect of wall-normal resolution

The effect of wall-normal resolution is shown in figure 17, where the bifurcation diagram with L_z is shown for $N_y = 97$ and $N_y = 129$. It appears that the use of $N_y = 97$ shows excellent agreement with that of $N_y = 129$, only except around $L_z/h \simeq 0.8$.

https://doi.org/10.1017/jfm.2018.1017 Published online by Cambridge University Press

Appendix B. Effect of reference length scale for attached eddies

In Townsend's attached eddy hypothesis (Townsend 1956, 1976), the length scale of each attached eddy is the distance from its centre to the wall (i.e. y). Hwang (2015) has shown that the spanwise size of the attached eddy is proportional to its

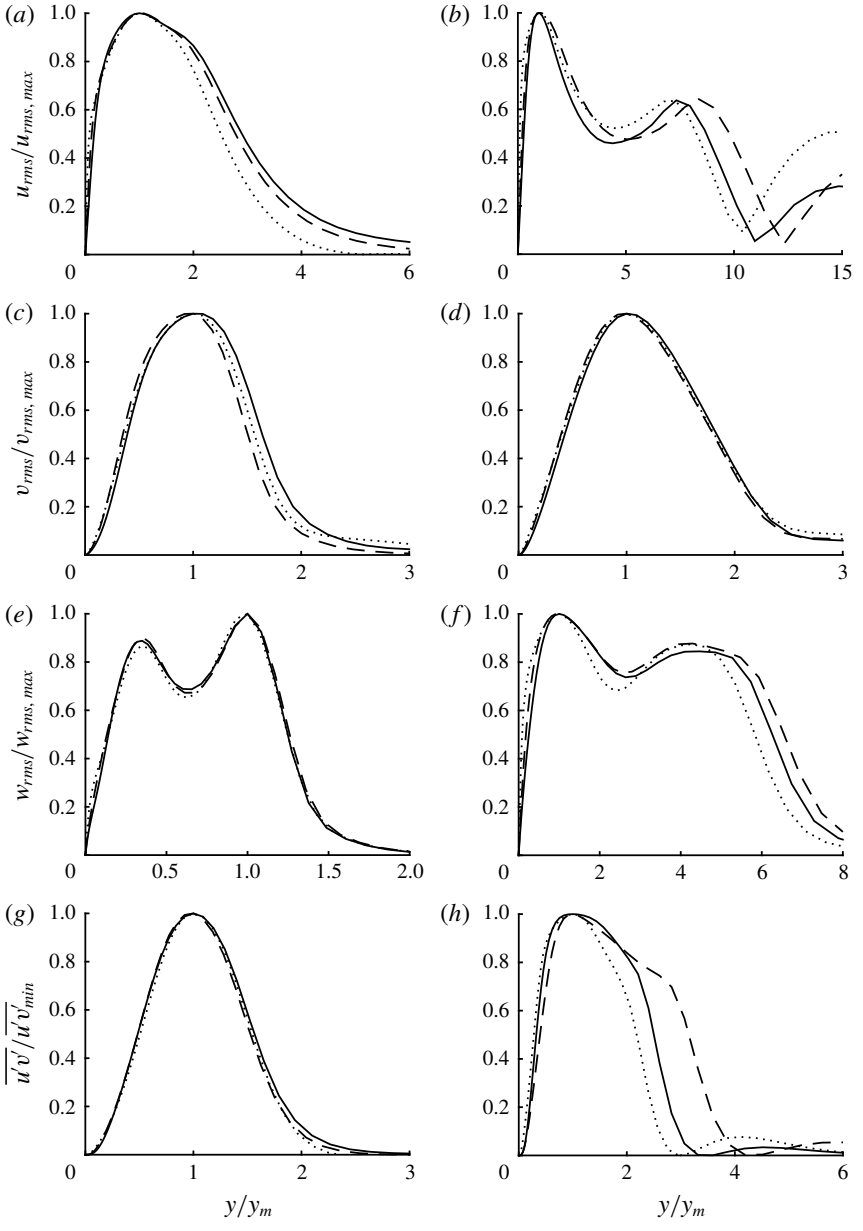


FIGURE 18. Normalised second-order statistics of (a,c,e,g) the lower- and (b,d,f,h) the upper-branch states with respect to the peak location of each profile, y_m: (a,b) streamwise, (c,d) wall-normal and (e,f) spanwise velocity and (g,h) Reynolds shear stress. Here: ——, $L_z/h = 0.375$; – – – –, $L_z/h = 0.5$; · · · · · ·, $L_z/h = 0.75$.

https://doi.org/10.1017/jfm.2018.1017 Published online by Cambridge University Press

centre height. Therefore, in the present study, the spanwise domain L_z has been used as the reference length scale, as shown in figure 10. However, the self-similarity in figure 10 remains almost unchanged if the statistics of the present exact solution of the overdamped simulation are rescaled with the distance from the wall. To demonstrate this, the normalised second-order statistics for the lower- and upper-branch states in figure 10 are scaled with the peak wall-normal location of each profile, y_m, and they are shown in figure 18. Reasonably good self-similarity is also observed as in figure 10.

REFERENCES

AFZAL, N. 1982 Fully developed turbulent flow in a pipe: an intermediate layer. *Ing.-Arch.* **52**, 355–377.

DEL ÁLAMO, J. C. & JIMÉNEZ, J. 2003 Spectra of the very large anisotropic scales in turbulent channels. *Phys. Fluids* **15**, L41.

DEL ÁLAMO, J. C. & JIMÉNEZ, J. 2006 Linear energy amplification in turbulent channels. *J. Fluid Mech.* **559**, 205–213.

DEL ÁLAMO, J. C., JIMÉNEZ, J., ZANDONADE, P. & MOSER, R. D. 2006 Self-similar vortex clusters in the turbulent logarithmic region. *J. Fluid Mech.* **561**, 329–358.

ALIZARD, F. 2015 Linear stability of optimal streaks in the log-layer of turbulent channel flows. *Phys. Fluids* **27**, 105103.

BEWLEY, T. R. 2014 *Numerical Renaissance: Simulation, Optimization, and Control*. Renaissance Press.

BUDANUR, N. B. & HOF, B. 2017 Heteroclinic path to spatially localized chaos in pipe flow. *J. Fluid Mech.* **827**, R1.

BUTLER, K. M. & FARRELL, B. F. 1993 Optimal perturbations and streak spacing in wall-bounded turbulent shear flow. *Phys. Fluids* **5**, 774–777.

CASSINELLI, A., DE GIOVANETTI, M. & HWANG, Y. 2017 Streak instability in near-wall turbulence revisited. *J. Turbul.* **18** (5), 443–464.

CHINI, G. P., MONTEMURO, B., WHITE, C. M. & KLEWICKI, J. 2017 A self-sustaining process model of inertial layer dynamics in high Reynolds number turbulent wall flows. *Phil. Trans. R. Soc. Lond.* **95**, 264504.

CHO, M., HWANG, Y. & CHOI, H. 2018 Scale interactions and spectral energy transfer in turbulent channel flow. *J. Fluid Mech.* **854**, 474–504.

COSSU, C., PUJALS, G. & DEPARDON, S. 2009 Optimal transient growth and very large scale structures in turbulent boundary layers. *J. Fluid Mech.* **619**, 79–94.

DEGUCHI, K. 2015 Self-sustaining states at Kolmogorov microscale. *J. Fluid Mech.* **781**, R6.

ECKHARDT, B. & ZAMMERT, S. 2018 Small scale exact coherent structures at large Reynolds numbers in plane Couette flow. *Nonlinearity* **31**, R66–R77.

FAISST, H. & ECKHARDT, B. 2004 Sensitive dependence on initial conditions in transition to turbulence. *J. Fluid Mech.* **504**, 343–352.

FUKAGATA, K., IWAMOTO, K. & KASAGI, N. 2002 Contribution of Reynolds stress distribution to the skin friction in wall-bounded flows. *Phys. Fluids* **14** (11), 13–17.

GIBSON, J. F., HALCROW, J. & CVITANOVIC, P. 2008 Visualizing the geometry of state space in plane Couette flow. *J. Fluid Mech.* **611**, 107–130.

GIBSON, J. F., HALCROW, J. & CVITANOVIC, P. 2009 Equilibrium and traveling-wave solutions of plane Couette flow. *J. Fluid Mech.* **638**, 243–266.

DE GIOVANETTI, M., HWANG, Y. & CHOI, H. 2016 Skin-friction generation by attached eddies in turbulent channel flow. *J. Fluid Mech.* **808**, 511–538.

DE GIOVANETTI, M., SUNG, H. J. & HWANG, Y. 2017 Streak instability in turbulent channel flow: the seeding mechanism of large-scale motions. *J. Fluid Mech.* **832**, 483–513.

HAMILTON, J. M., KIM, J. & WALEFFE, F. 1995 Regeneration mechanisms of near-wall turbulence structures. *J. Fluid Mech.* **287**, 317–348.

https://doi.org/10.1017/jfm.2018.1017 Published online by Cambridge University Press

HEAD, M. R. & BANDYOPADHAY, P. 1981 New aspects of turbulent boundary-layer structure. *J. Fluid Mech.* **107**, 297–338.

HELLSTÖM, L. H. O., MARUSIC, I. & SMITS, A. J. 2016 Self-similarity of the large-scale motions in turbulent pipe flow. *J. Fluid Mech.* **792**, R1.

HUTCHINS, N. & MARUSIC, I. 2007 Evidence of very long meandering features in the logarithmic region of turbulent boundary layers. *J. Fluid Mech.* **579**, 1–28.

HWANG, Y. 2013 Near-wall turbulent fluctuations in the absence of wide outer motions. *J. Fluid Mech.* **723**, 264–288.

HWANG, Y. 2015 Statistical structure of self-sustaining attached eddies in turbulent channel flow. *J. Fluid Mech.* **723**, 264–288.

HWANG, Y. & BENGANA, Y. 2016 Self-sustaining process of minimal attached eddies in turbulent channel flow. *J. Fluid Mech.* **795**, 708–738.

HWANG, Y. & COSSU, C. 2010*a* Linear non-normal energy amplification of harmonic and stochastic forcing in the turbulent channel flow. *J. Fluid Mech.* **664**, 51–73.

HWANG, Y. & COSSU, C. 2010*b* Self-sustained process at large scales in turbulent channel flow. *Phys. Rev. Lett.* **105**, 044505.

HWANG, Y. & COSSU, C. 2011 Self-sustained processes in the logarithmic layer of turbulent channel flows. *Phys. Fluid* **23**, 061702.

HWANG, Y., WILLIS, A. P. & COSSU, C. 2016 Invariant solutions of minimal large-scale structures in turbulent channel flow for Re_τ up to 1000. *J. Fluid Mech.* **802**, R1.

JEONG, J., BENNEY, F., SCHOPPA, W. & KIM, J. 1997 Coherent structures near the wall in a turbulent channel flow. *J. Fluid Mech.* **332**, 185–214.

JEONG, J. & HUSSAIN, F. 1995 On the identification of a vortex. *J. Fluid Mech.* **285**, 69–94.

JIMÉNEZ, J. & PINELLI, A. 1999 The autonomous cycle of near-wall turbulence. *J. Fluid Mech.* **389**, 335–359.

JIMÉNEZ, J. & SIMENS, M. P. 2001 Low-dimensional dynamics of a turbulent wall flow. *J. Fluid Mech.* **435**, 81–91.

VON KÁRMÁN, T. 1930 Mechanische aehnlichkeit und turbulenz. *Nachr. Ges. Wiss. Göttingen, Math. Phys. Kl.* 58–68; English translation *NACA TM* 611.

KAWAHARA, G. & KIDA, S. 2001 Periodic motion embedded in plane Couette turbulence: regeneration cycle and burst. *J. Fluid Mech.* **449**, 291–300.

KIM, J. & HUSSAIN, F. 1993 Propagation velocity of perturbations in turbulent channel flow. *Phys. Fluids* **5**, 695–706.

KIM, K. C. & ADRIAN, R. 1999 Very large-scale motion in the outer layer. *Phys. Fluids* **11** (2), 417–422.

KLINE, S. J., REYNOLDS, W. C., SCHRAUB, F. A. & RUNSTADLER, P. W. 1967 The structure of turbulent boundary layers. *J. Fluid Mech.* **30**, 741–773.

KOVASZNAY, L. S. G., KIBENS, V. & BLACKWELDER, R. F. 1970 Large-scale motion in the intermittent region of a turbulent boundary layer. *J. Fluid Mech.* **41**, 283–325.

LEE, M. & MOSER, R. D. 2019 Spectral analysis of the budget equation in turbulent channel flows at high Reynolds number. *J. Fluid Mech.* **860**, 886–938.

MARUSIC, I. & MONTY, J. P. 2019 Attached eddy model of wall turbulence. *Annu. Rev. Fluid Mech.* **51**, 49–74.

MARUSIC, I., MONTY, J. P., HULTMARK, M. & SMITS, A. J. 2013 On the logarithmic region in wall turbulence. *J. Fluid Mech.* **716**, R3.

MCKEON, B. J. & SHARMA, A. S. 2010 A critical-layer framework for turbulent pipe flow. *J. Fluid Mech.* **658**, 336–382.

MELLIBOVSKY, F. & ECKHARDT, B. 2011 Takens–Bogdanov bifurcation of travelling-wave solutions in pipe flow. *J. Fluid Mech.* **670**, 96–129.

MOARREF, R., SHARMA, A. S., TROPP, J. A. & MCKEON, B. J. 2013 Model-based scaling of the streamwise energy density in high-Reynolds-number turbulent channels. *J. Fluid Mech.* **734**, 275–316.

MOSER, R. D., KIM, J. & MANSOUR, N. N. 1999 Direct numerical simulation of turbulent channel flow up to $Re = 590$. *Phys. Fluids* **11**, 943–945.

https://doi.org/10.1017/jfm.2018.1017 Published online by Cambridge University Press

NAGATA, M. 1990 Three-dimensional finite-amplitude solutions in plane Couette flow: bifurcation from infinity. *J. Fluid Mech.* **217**, 519–527.

NEELAVARA, S. A., DUGUET, Y. & LUSSEYRAN, F. 2017 State space analysis of minimal channel flow. *Fluid Dyn. Res.* **49**, 035511.

PARK, J., HWANG, Y. & COSSU, C. 2011 On the stability of large-scale streaks in the turbulent Couette and Poiseuille flows. *C. R. Méc.* **339** (1), 1–5.

PERRY, A. E. & CHONG, M. S. 1982 On the mechanism of turbulence. *J. Fluid Mech.* **119**, 173–217.

PERRY, A. E., HENBEST, S. & CHONG, M. S. 1986 A theoretical and experimental study of wall turbulence. *J. Fluid Mech.* **165**, 163–199.

PERRY, A. E. & MARUSIC, I. 1995 A wall-wake model for the turbulence structure of boundary layers. Part 1. Extension of the attached eddy hypothesis. *J. Fluid Mech.* **298**, 361–388.

PRANDTL, L. 1925 Bericht über doe emtstejimg der turbulenz. *Z. Angew. Math. Mech.* **5**, 136–139.

PUJALS, G., GARCÍA-VILLALBA, M., COSSU, C. & DEPARDON, S. 2009 A note on optimal transient growth in turbulent channel flows. *Phys. Fluids* **21**, 015109.

RAWAT, S., COSSU, C., HWANG, Y. & RINCON, F. 2015 On the self-sustained nature of large-scale motions in turbulent Couette flow. *J. Fluid Mech.* **782**, 515–540.

RAWAT, S., COSSU, C. & RINCON, F. 2016 Travelling-wave solutions bifurcating from relative periodic orbits in plane Poiseuille flow. *C. R. Méc.* **344**, 448–455.

SCHOPPA, W. & HUSSAIN, F. 2002 Coherent structure generation in near-wall turbulence. *J. Fluid Mech.* **453**, 57–108.

SMAGORINSKY, J. 1963 General circulation experiments with the primitive equations: I. The basic equations. *Mon. Weath. Rev.* **91**, 99–164.

SREENIVASAN, K. R. & SAHAY, A. 1997 The persistence of viscous effects in the overlap region and the mean velocity in turbulent pipe and channel flows. In *Self-Sustaining Mechanisms of Wall Turbulence* (ed. R. Panton), pp. 253–272. Computational Mechanics.

TENNEKES, H. & LUMLEY, J. L. 1967 *A First Course in Turbulence*. MIT Press.

TOWNSEND, A. A. 1956 *The Structure of Turbulent Shear Flow*, 1st edn. Cambridge University Press.

TOWNSEND, A. A. 1976 *The Structure of Turbulent Shear Flow*, 2nd edn. Cambridge University Press.

VISWANATH, D. 2007 Recurrent motions within plane Couette turbulence. *J. Fluid Mech.* **580**, 339–358.

WALEFFE, F. 1997 On a self-sustaining process in shear flows. *Phys. Fluids* **9**, 883–900.

WALEFFE, F. 1998 Three-dimensional coherent states in plane shear flows. *Phys. Rev. Lett.* **81**, 4140–4143.

WALEFFE, F. 2001 Exact coherent structures in channel flow. *J. Fluid Mech.* **435**, 93–102.

WALEFFE, F. 2003 Homotopy of exact coherent structures in plane shear flows. *Phys. Fluids* **15**, 1517–1534.

WEDIN, H. & KERSWELL, R. R. 2004 Exact coherent structures in pipe flow: travelling wave solutions. *J. Fluid Mech.* **508**, 333–371.

WILLIS, A. P., CVITANOVIC, P. & AVILA, M. 2013 Revealing the state space of turbulent pipe flow by symmetry reduction. *J. Fluid Mech.* **721**, 514–540.

WILLIS, A. P., CVITANOVIC, P. & AVILA, M. 2016 Symmetry reduction in high dimensions, illustrated in a turbulent pipe. *Phys. Rev.* E **93**, 022204.

WILLIS, A. P., HWANG, Y. & COSSU, C. 2010 Optimally amplified large-scale streaks and drag reduction in the turbulent pipe flow. *Phys. Rev.* E **82**, 036321.

WOODCOCK, J. D. & MARUSIC, I. 2015 The statistics behaviour of attached eddies. *Phys. Fluids* **27**, 015104.

YANG, Q., WILLIS, A. P. & HWANG, Y. 2018 Energy production and self-sustained turbulence at the Kolmogorov scale in Couette flow. *J. Fluid Mech.* **834**, 531–554.

https://doi.org/10.1017/jfm.2018.1017 Published online by Cambridge University Press